Evolution and transition mechanisms of internal swirling flows with tangential entry

Yanxing Wang, Xingjian Wang, and Vigor Yang[a)]
School of Aerospace Engineering, Georgia Institute of Technology, Atlanta, Georgia 30332, USA

(Received 21 August 2017; accepted 12 December 2017; published online 16 January 2018)

The characteristics and transition mechanisms of different states of swirling flow in a cylindrical chamber have been numerically investigated using the Galerkin finite element method. The effects of the Reynolds number and swirl level were examined, and a unified theory connecting different flow states was established. The development of each flow state is considered as a result of the interaction and competition between basic mechanisms: (1) the centrifugal effect, which drives an axisymmetric central recirculation zone (CRZ); (2) flow instabilities, which develop at the free shear layer and the central solid-body rotating flow; (3) the bouncing and restoring effects of the injected flow, which facilitate the convergence of flow on the centerline and the formation of bubble-type vortex breakdown; and (4) the damping effect of the end-induced flow, which suppresses the development of the instability waves. The results show that the CRZ, together with the free shear layer on its surface, composes the basic structure of swirling flow. The development of instability waves produces a number of discrete vortex cores enclosing the CRZ. The azimuthal wave number is primarily determined by the injection angle. Generally, the wave number is smaller at a higher injection angle, due to the reduction of the perimeter of the free shear layer. At the same time, the increase in the Reynolds number facilitates the growth of the wave number. The end-induced flow tends to reduce the wave number near the head end and causes a change in wave number from the head end to the downstream region. Spiral-type vortex breakdown can be considered as a limiting case at a high injection angle, with a wave number equal to 0 near the head end and equal to 1 downstream. At lower Reynolds numbers, the bouncing and restoring effect of the injected flow generates bubble-type vortex breakdown. *Published by AIP Publishing.* https://doi.org/10.1063/1.5001073

I. INTRODUCTION

One of the most significant characteristics of swirling flow, the central recirculation zone (CRZ), plays an important role in many engineering applications, such as fuel mixing and flame stabilization in combustion devices.[1–3] Although considerable efforts have been applied to study this phenomenon, the mechanisms and characteristics of the CRZ remain to be further explored; the challenge lies primarily in the complexity of the interactions of various underlying mechanisms, subject to a broad range of flow parameters.

There are typically two different kinds of CRZs created in swirling flow: One is produced by vortex breakdown, and the other is caused by strong centrifugal force. Vortex breakdown commonly takes place at a lower swirl level. When the adverse pressure gradient along the centerline cannot be balanced by the kinetic energy of the flow, a recirculation zone, referred to as vortex breakdown, is developed. The technical importance of vortex breakdown has spurred extensive studies since it was first described by Peckham and Atkinson.[4] Faler and Leibovich[5] identified up to seven distinct vortex breakdown modes, via flow visualization at a variety of Reynolds numbers and swirl numbers. More recently, the control of vortex breakdown using wall rotation in swirling pipe flows was investigated by Dennis *et al.*[6]

In industrial applications such as the swirl injector of the gas turbine,[7,8] the most commonly observed vortex breakdown is of the "bubble" and "spiral" types. One prerequisite for vortex breakdown is the formation of an axisymmetric vortex core with intensified vorticity magnitude on the centerline;[9] this characteristic behavior distinguishes vortex breakdown from other recirculating flows. Vortex breakdown is such a highly nonlinear phenomenon that there is no simple set of parameters that can specify it clearly. A recent review on this subject was given by Lucca-Negro and O'Doherty.[9]

When the swirl level is raised to such a high level that the centrifugal effect becomes dominant over the other effects, the flow evolves into another state, which is characterized by a bubble- or column-like CRZ. This kind of a CRZ is commonly observed in the swirl injector of the liquid rocket engine,[10,11] and only occurs when the swirl number S exceeds a critical value S_{crit}.[1,2] Gupta *et al.*[2] found that S_{crit} is about 0.6 for flows in straight tubes.

Harvey[12] performed experiments on swirling flow within a divergent tube. Varying the swirl level of the injected flow, he observed several distinct flow states. At a very low swirl level, flow was stable, and no recirculation was established. As the flow swirl was increased up to a certain value, the commonly recognized vortex breakdown appeared. With a further increase in the swirl level, vortex breakdown shifted to another state and a columnar CRZ was created. Harvey[12] conducted the first study identifying the transitions between different

[a)]Author to whom correspondence should be addressed: vigor.yang@aerospace.gatech.edu

recirculation zones. In general, the columnar recirculation zone exhibits patterns similar to those of the bubble-type vortex breakdown. In industrial applications, in particular, these two kinds of recirculation zones are always considered to be of the same type. However, from the perspective of fundamental definitions and governing mechanisms, they belong to distinct flow states, and it is not yet clear how these different flow states are related. Inadequate understanding of the underlying physics impedes the use of swirling flows in real-world applications.

Previous experimental measurements[1,2,13] have shown that the columnar CRZ is enveloped by a free shear layer, across which the tangential and axial velocities change significantly. The sharp velocity change across the free shear layer, as well as the swirl motion of the central flow, provides the potential for instability waves to develop. Wang and Yang[14] found that when the Reynolds number and injection angle meet certain criteria, instability waves develop, and the axisymmetric free shear layer breaks up into several identical spiral vortex cores. With an increase in the injection angle, the azimuthal wave number decreases. It is known that the most common types of vortex breakdown (bubble type and spiral type) feature an axisymmetric preceding vortex core on the centerline. If the axisymmetric vortex core is considered as the limiting case of flow instabilities with the azimuthal wave number $m = 0$, then vortex breakdown may take place by adjusting the Reynolds number and injection angle to reduce m to zero. Here m refers to the number of discrete vortices aligned along the perimeter of the free shear layer when azimuthal instability occurs. This consideration suggests the hypothesis that the azimuthal instability waves serve as a bridge connecting the flow state with a columnar CRZ at a high swirl level and the state with vortex breakdown at a low swirl level. The variation in the azimuthal wave number brings about the transition from one type to the other.

In order to validate such hypothesis, in the present work, we design a numerical model to simulate the swirling flow in a cylindrical chamber, as shown schematically in Fig. 1. Flow is injected into the cylinder through a ring entrance on the sidewall near the head end. Flow swirl is introduced aerodynamically by adjusting the injection angle. In this paper, we build on our previous study,[14] which numerically examined the instability waves that develop in the swirling flow in a cylindrical chamber with a slip head end. In that paper, we found that the azimuthal wave number is primarily determined by the injection angle. The increase in the injection angle causes the shrinking of the free shear layer, which leads to a decrease in the wave number.

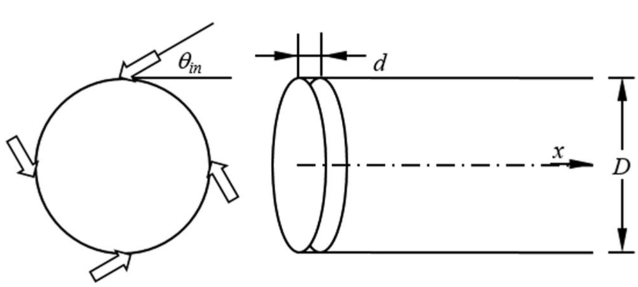

FIG. 1. Configuration of the cylindrical container with a ring entry.

An important but often unrecognized issue in swirling flows is the friction on the stationary head end. In the boundary layer on the head end, the equilibrium between the radial pressure gradient and the centrifugal force is broken. The excessive pressure gradient drives the fluid in the boundary layer to the center region and gives rise to a jet-like flow along the centerline. The jet flow interacts with the CRZ and the instability waves and makes the behaviors of the CRZ more sophisticated. To the best of our knowledge, little work has been published in this area.

An aim of the current study is to extend our previous work[14] to swirling flow with the influence of a nonslip head end. By studying the flow characteristics at various swirl levels and Reynolds numbers, we attempt to identify the links between different flow states from the perspective of instability waves and provide a general theory for the distinctive types of the CRZ.

This paper is organized as follows. In Sec. II, detailed descriptions of the physical model is presented. In Sec. III, the numerical model and approaches are provided. The results are discussed in Sec. IV. Section V presents the conclusions.

II. PHYSICAL MODEL

A schematic of the swirl configuration is shown in Fig. 1. The present geometry includes a long cylinder of diameter D with a ring slit on the head, through which the fluid is injected into the chamber. The width of the entrance is d. The fluid is injected into the chamber through the entrance with uniform radial velocity $U_{r,in}$ and tangential velocity $U_{\theta,in}$. The injection angle is defined as the angle between the injection velocity vector and the tangent of the cylindrical chamber and is expressed as $\theta_{in} = \tan^{-1}(U_{r,in}/U_{\theta,in})$. The radial velocity component can be acquired from $U_{\theta,in}$ and θ_{in}. Thus, a complete description of the swirling flow in the cylinder includes D, d, θ_{in}, $U_{\theta,in}$, and ν, where ν is the kinematic viscosity of the fluid in the chamber.

Since swirl effects are closely related to the tangential velocity at the entrance, we choose the tangential velocity of injected flow $U_{\theta,in}$ and the cylinder diameter D as the characteristic variables. The Reynolds number is defined as

$$\mathrm{Re}_\theta = \frac{U_{\theta,in} D}{\nu}. \tag{1}$$

Conventionally, the Reynolds number is defined based on the mean axial velocity in the cylinder as $\mathrm{Re}_x = \overline{u}_x D/\nu$. The relationship between the tangential and the conventional Reynolds number based on the mean axial velocity is

$$\mathrm{Re}_x = \frac{4d}{D} \tan\theta_{in} \cdot \mathrm{Re}_\theta. \tag{2}$$

In this study, we only consider laminar flows, with Re_θ ranging from 100 to 3000. In the simulation, the velocity and length scales are normalized with the tangential velocity of the injected flow $U_{\theta,in}$ and the radius of the cylindrical chamber R. In the nondimensional form, $U_{\theta,in} = 1$, $D = 2$, the controlling parameters for the present configuration reduces to d, θ_{in}, and Re_θ. The angular momentum carried by unit volume of the fluid through the entrance is

$$M = U_{\theta,in} D/2 = 1. \tag{3}$$

TABLE I. Swirl number of injected flow with various vane angles.

θ_{in} (deg)	10	20	30	45	55	60	75
S_{in}	14.18	6.87	4.33	2.50	1.75	1.44	0.67

The volume flow rate injected into the chamber is

$$\dot{V} = U_{\theta,in} \tan\theta_{in} \cdot \pi D d = 2\pi d \tan\theta_{in}. \tag{4}$$

The immediate consequence of increasing the injection angle θ_{in} is an increase in the volume flow rate and the angular momentum flux into the chamber. The swirl level, characterized by the swirl number, is defined as

$$S = \frac{\displaystyle\int_A \rho u_\theta r \cdot u_x dA}{D/2 \cdot \displaystyle\int_A \rho u_x \cdot u_x dA}, \tag{5}$$

where A is the cross sectional area at any axial location of the cylinder. In the present configuration, the fluid is injected into the chamber with zero axial velocity, so we must define an equivalent swirl number to avoid dividing by zero axial velocity in estimating the swirl number of the injected flow. An approximate method is to employ the averaged axial velocity $\bar{u}_x$ obtained from the volume flow rate injected into the chamber and assume that the angular momentum is perfectly conserved. The swirl number of the injected flow is thus defined as

$$S_{in} = \frac{R}{2d}\frac{1}{\tan\theta_{in}}, \tag{6}$$

where $R = 1$ in the nondimensional form. This expression implies that for a given geometry the injection swirl number S_{in} is inversely proportional to the tangent of the injection angle θ_{in}. Increasing the injection angle θ_{in} leads to a decrease in the swirl level of the injected flow. This is because the increase in θ_{in} increases the axial fluxes of both angular momentum and axial momentum. The ratio of these two fluxes, however, decreases. This conclusion is only valid for the injected flow in a limited upstream regime, since viscous dissipation tends to decrease the flow swirl, and the variation of the swirl number also depends on the specific flow characteristics. In the present study, the nondimensional entrance width d is fixed at 0.2. The swirl numbers of the injected flow at various angles considered in the present study are listed in Table I.

III. GOVERNING EQUATIONS AND NUMERICAL METHODS

Under the assumption that the flow is laminar, three-dimensional, and incompressible, the non-dimensional conservation equations based on the tangential velocity of injected flow and the chamber diameter can be written as

$$\nabla \cdot \mathbf{u} = 0, \tag{7}$$

$$\frac{\partial \mathbf{u}}{\partial t} + \mathbf{u} \cdot \nabla \mathbf{u} = -\nabla p + \frac{2}{\mathrm{Re}_\theta}\nabla^2 \mathbf{u}, \tag{8}$$

where Re_θ is the Reynolds number, $\mathbf{u}$ is the velocity vector, and p is the pressure.

In this paper, a finite element solution for three-dimensional incompressible viscous flow is considered. Discretization in space is carried out by the Galerkin weighted residual method. Time advancement is achieved by the velocity correction method (explicit forward Euler) of Kovacs and Kawahara.[15] The method gives results of the second-order accuracy in both time and space.

The axial length of the computational domain is 30 times as long as the cylinder radius. For laminar flow, it is long enough to render inconsequential influence on the interior flow of the downstream boundary. There are 4205 grid nodes on each cross section and 300 grid nodes in the axial direction. Through the width of the slit entrance, 12 grid nodes are used, which is sufficient to resolve the flow at the Reynolds numbers considered in this study. For different cases, the distribution of grid nodes is adjusted according to the gradients of flow quantities.

A flow with uniform axial velocity and zero azimuthal velocity are used as the initial conditions. Calculations are conducted over an extended time period to allow the flow to reach a stationary state at which all variables change periodically with time. Data acquisition and analysis are performed afterwards.

The details of the numerical method, with validation tests, are given in the study Wang *et al.*[16,17]

IV. RESULTS AND DISCUSSION

In swirling flow, the centrifugal force exerted on fluid particles, which is roughly proportional to the square of the azimuthal velocity, is balanced by the radial pressure gradient. The surface friction of the stationary head end creates a boundary layer, in which the azimuthal velocity and corresponding centrifugal force decrease significantly. However, the radial pressure gradient in the boundary layer stays approximately the same as that outside. Thus, the equilibrium between the radial pressure gradient and the centrifugal force is broken, and the excessive pressure gradient drives the fluid in the boundary layer to the central region and forms a jet-like flow on the centerline. It should be noted that this boundary layer is different from the Ekmann layer formed on the rotating solid surface in stationary flow.[18] An extensive analysis of the flows in the same geometry but with a slip head end is given by Wang and Yang.[14] In that work, the flow characteristics of each state as well as the onset of instability waves and mode selection are discussed. As an extension of that work, the present study takes into account the influence of friction on the head end and deals with the flows in a practical cylindrical chamber. The mechanisms are more complex.

For a given configuration, the flow evolution in the chamber is determined by the injection swirl number S_{in} and the tangential Reynolds number Re_θ. In the following analysis, the case with least complexity, the axisymmetric basic flow without the instability wave, will be discussed first. This kind of flow generally occurs at a high swirl level and low Reynolds number. The instability waves developing in the free shear layer at a lower swirl level will then be discussed. Overall, the injection angle θ_{in} increases from 10° to 75°. Correspondingly, the injection swirl number S_{in} decreases from

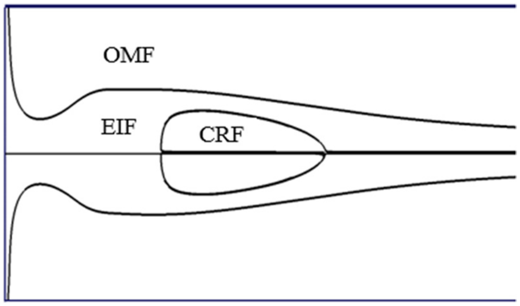

FIG. 2. Structure of swirling flow with the columnar CRZ in the cylindrical chamber: OMF: outer main flow; EIF: end-induced flow; CRF: central recirculating flow.

14.18 to 0.67 (Table I). The azimuthal Reynolds number covers a range of 100-3000. We restrict our present study to laminar flows.

A. Axisymmetric central recirculation zone (CRZ) at high swirl level and low Reynolds number

At a high swirl level, the centrifugal effect is dominant over the other effects, and flow is characterized by an axisymmetric CRZ. When the fluid is injected into the chamber, the strong centrifugal force due to high swirl drives the flow outward and forces it to travel downstream along the sidewall in a spiral path. This flow motion creates an axisymmetric column, or bubble-like recirculation zone, along the centerline. In the boundary layer on the head end, the fluid is driven to the central region by the unbalanced radial pressure gradient, and then turns downstream along the centerline. This axial flow originating from the head end boundary layer is referred to as the end-induced flow. When travelling downstream, the end-induced flow envelops the CRZ and separates the CRZ from the outer main flow. As shown in Fig. 2, the flow in the chamber can be decomposed into three parts: the outer main flow, the end-induced flow, and the central recirculating flow. We will show in the following discussion that although the velocity magnitude of the end-induced flow is small, it has a strong influence on the downstream flow.

The flow at $\theta_{in} = 20°$ and $Re_\theta = 300$ is used as an example to demonstrate the basic flow patterns, as shown in Fig. 3. When the Reynolds number is not too high, the flow stays stable to azimuthal disturbances, and the flow patterns remain axisymmetric. Figures 3(a) and 3(b) show the typical three-dimensional streamlines of the central recirculating flow and the outer downstream traveling flow, respectively. In steady flow, the streamlines coincide with the trajectories of the fluid particles. The streamlines in these two figures show that both the outer and central flows travel in a spiral manner. In Fig. 3(c), which shows the projected streamlines on the x-y plane, the bubble-like central recirculating zone can be clearly identified. Comparing with the flow under the same conditions in the chamber with the slip head end,[14] the end-induced flow detaches the CRZ from the head end and drives the upstream stagnation point of the CRZ quite a distance downstream. The length and radius of the CRZ decrease significantly with the influence of the end-induced flow. The contours of axial velocity are shown in Fig. 3(d). In the outer region, the high velocity magnitudes (red and orange) indicate the passage through which the injected flow travels downstream. In the central region, the axial velocity is smaller than that in the outer region. In particular, in the CRZ, the axial velocity becomes negative around the centerline. Figure 3(e) shows the contours of azimuthal velocity. In the central region occupied by the CRZ and the end-induced flow, the contour lines of azimuthal velocity are roughly uniformly distributed and are largely parallel to the centerline. This pattern suggests that the central region takes on the behavior of a solid body rotation on the centerline. In our previous work with the slip head end,[14] the

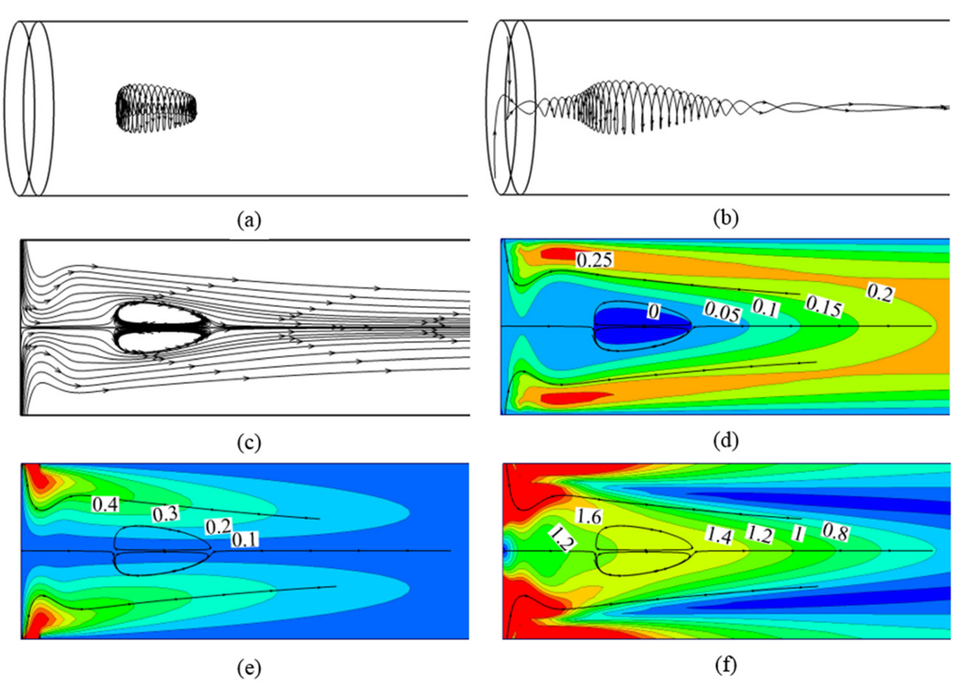

FIG. 3. Overview of swirling flow with the columnar CRZ in the cylindrical chamber at $\theta_{in} = 20°$ and $Re_\theta = 300$: (a) typical streamlines in the CRZ; (b) typical streamlines outside the CRZ; (c) projected streamlines on the x-y plane; (d) contours of axial velocity u_x on the x-y plane; (e) contours of azimuthal velocity u_θ on the x-y plane; (f) contours of vorticity magnitude $|\omega|$ on the x-y plane.

central region is basically occupied by a recirculating flow, the motion of which is driven by the outer main flow through a free shear layer.

In the present study, the surface friction on the head end creates an end-induced flow, which separates the CRZ from the outer flow. Since the end-induced flow originates from the boundary layer on the head end, the azimuthal velocity is much lower than that of the outer flow. Therefore, we consider both the end-induced flow and the central recirculating flow as the central flows in the present paper. The term "central regions" denotes the regions occupied by these two flows. To facilitate discussion, it is reasonable to use the line across which the azimuthal velocity changes abruptly to define the interface between the central flows and the outer flow. In practice, it is more convenient to use the vorticity field to find the interface. Figure 3(f) shows the contours of vorticity magnitude on the x-y plane. A free shear layer with concentrated vorticity magnitude is developed from the head end, and this serves as the interface separating the central flows from the outer flow. This free shear layer is created by the differences in the azimuthal and axial velocities between the outer main flow and the end-induced flow. The CRZ is enclosed by the end-induced flow, and both the CRZ and the end-induced flow have much lower swirl and axial velocities, so no free shear layer with sharp velocity change develops at the surface of the CRZ. One significant difference from the flow in the chamber with the slip head end[14] lies in the fact that the CRZ is separated from the head end and the outer main flow by the end-induced flow, and the free shear layer shifts to the interface between the outer main flow and the end-induced flow.

The profiles of azimuthal and axial velocities at different axial locations are given in Figs. 4(a) and 4(b). Two turning points can be observed in the azimuthal velocity on the curve in the upstream region of the CRZ. Between these two points, the azimuthal velocity decreases significantly, from the maximum azimuthal velocity of the outer flow to the lower azimuthal velocity of the central flows. The region where the azimuthal velocity decreases abruptly is right where the free shear layer develops at the interface between the outer main flow and the end-induced flow. In a chamber with the slip head end,[14] the azimuthal velocity of the outer flow satisfies the conservation of angular momentum in the vicinity of the entrance. In the present configuration, however, the non-slip condition on the head end dissipates the angular momentum and breaks the conservation law near the head end. Below the free shear layer, a linear relationship between the azimuthal velocity and the radial location is observed in the central region. It confirms the conclusion from Fig. 3 that the flows in the central region take on a solid-body rotation.

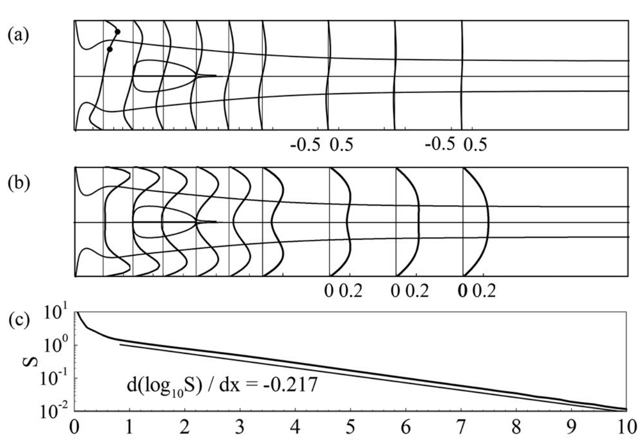

FIG. 4. Profiles of (a) azimuthal and (b) axial velocity components at different axial locations and (c) axial variation of the swirl number at θ_{in} = 20° and Re_θ = 300. Two solid dots in (a) indicating the turning points of azimuthal velocity.

The central flows are driven by the outer flow through the free shear layer. On the other curves in this figure, only one turning point can be observed near the interface of the outer main flow and the end-induced flow, and this means that the free shear layer only exists in a limited upstream region and does not expand far downstream, due to viscous diffusion and dissipation.

The azimuthal velocity decreases as the flow travels downstream. At $x = 3x_{end}$, where x_{end} is the axial coordinate of the downstream stagnation point of the CRZ, the azimuthal velocity almost vanishes. The distributions of axial velocity are shown in Fig. 4(b), which indicates that the axial velocity has a peak inside the outer flow at each axial location. As the flow travels downstream, the position of the peak eventually shifts toward the centerline. At the interface between the outer main flow and the end-induced flow, the axial velocity changes sharply. Through this interface, the axial momentum is transferred from the outer main flow to the central flows. The creation of the free shear layer is therefore attributed not only to the difference in azimuthal velocity between the outer and central flows but also to the difference in axial velocity. In the area between the head end and the CRZ, which is occupied by the end-induced flow, the magnitude of axial velocity is much smaller than in the outer main flow. This is because the end-induced flow comes from the boundary layer on the head end, where the volume flow rate is much smaller than that of the main flow. As a result of the low injection angle, the end-induced flow is not strong enough to form a jet-like flow on the centerline. The comparison of Figs. 4(a) and 4(b) indicates that the viscous dissipation restricts the free shear layer at the interface to a limited upstream region. As flow travels downstream, the interface is smeared, and the end-induced flow combines with the outer main flow.

Figure 4(c) shows the axial variation of the swirl number for the present flow. The magnitude of the swirl number is given in the logarithmic scale. Due to viscous dissipation, the swirl number decreases monotonically from the head end to the far downstream region. For flows in the chamber with the slip head end,[14] it was found that the curve can be decomposed into two straight lines connecting at the end of the CRZ. In the present case, the end-induced flow smears the discontinuity of the curve slope and makes log$S$ linearly dependent on the axial coordinates, with a constant slope throughout the domain. However, the effect of end-induced flow is reduced at a higher Reynolds number. We show in the following discussion that the curve appears as two connecting straight lines at higher Reynolds numbers. This linear relationship between log$S$ and x provides strong evidence that the columnar CRZ

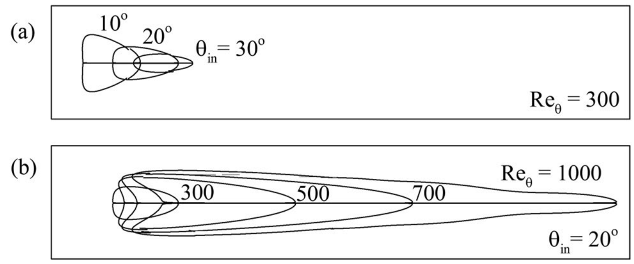

FIG. 5. Profiles of the CRZ on the x-y plane at different injection angles and Reynolds numbers: (a) Re_θ = 300; (b) θ_{in} = 20°.

is a quasi-linear phenomenon governed by swirl dissipation. It is known that the recirculation zone only appears when the local swirl number exceeds a critical value, which is around 0.6,[2] but the swirl number is not the only criterion. In the current flow, in the region between the head end and the CRZ, the swirl number is higher than the critical value, but this area is occupied by the end-induced flow, which drives the CRZ downstream.

In the present configuration, the behaviors of the CRZ are exclusively determined by the injection angle and the Reynolds number. A higher injection angle pushes the free shear layer closer to the centerline and narrows the passage of the end-induced flow. As a result, the axial velocity of the end-induced flow is higher; that is, the end-induced flow is stronger. On the other hand, a higher Reynolds number causes a thinner boundary layer on the head end. According to the conservation of mass, the axial velocity of the end-induced flow is lower. Figure 5 shows comparisons of the profiles of the CRZs at different injection angles and Reynolds numbers. As shown in Fig. 5(a), at Re_θ = 300, the increased injection angle not only strengthens the end-induced flow, which drives the CRZ farther downstream, but also squeezes the lateral radius of the CRZ. The effects of the Reynolds number are relatively more complex. At a higher Reynolds number, the viscous dissipation rate in swirl is lower, so the CRZ extends downstream longer. At the same time, the boundary layer on the inner side wall and the passage of the outer main flow are thinner at a higher Reynolds number, so the radial expansion of the CRZ is larger. In swirling flow at a high Reynolds number, the inverse flow in the CRZ has a tendency to deviate from the centerline, which shifts the upstream stagnation point of the CRZ downstream. Therefore, although the end-induced flow is weaker at a higher Reynolds number, the upstream stagnation point of the recirculation zone is located farther downstream.

It is known that the columnar CRZ ends at the position where S becomes smaller than S_c.[2] Therefore, the axial position of the downstream stagnation point of the CRZ x_{end} largely reflects the resistance of the flow to swirl dissipation. A higher Reynolds number permits a lower dissipation rate, and a higher injection angle has a larger flow rate of angular momentum, so both of them lead to a longer recirculation zone. Figure 6 shows the dependence of x_{end} on the Reynolds number Re_θ and the injection angle θ_{in}. The horizontal and vertical coordinates are given in the logarithmic scale in the figures. For flows in the chamber with the slip head end, the expression $x_{end} = c\,Re_\theta^a\,\theta_{in}^b$ was obtained.[14] However, this figure shows that in the chamber with the viscous head end, this relationship

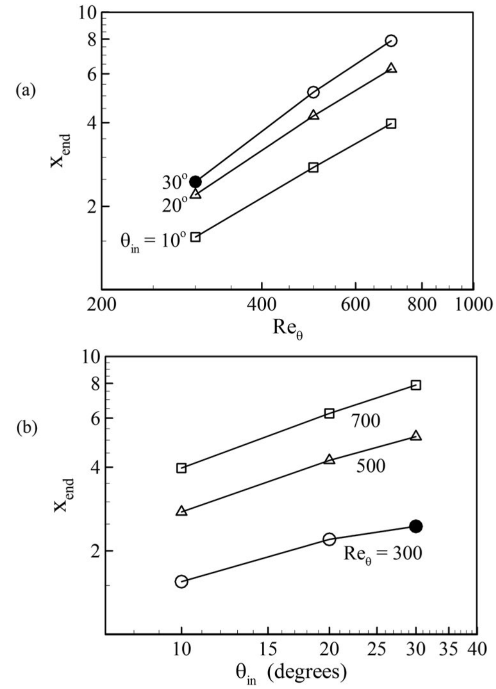

FIG. 6. Dependence of the end coordinate of the CRZ on the (a) Reynolds number Re_θ and (b) injection angle θ_{in}.

does not hold at θ_{in} = 30° and Re_θ = 300. The computational value of x_{end} is smaller than that predicted by the logarithmic linear expression. This phenomenon is caused by the restoring effect of the Coriolis force in swirling flow[19] and the bouncing effect of the injected flow. The end-induced flow deviates from the centerline at the upstream stagnation point of the CRZ, and travels along the surface of the recirculation zone, but the Coriolis force in the swirling system tends to return the fluid particles back to the centerline before the swirl number decreases to the critical value. At a lower Reynolds number, the boundary layer on the head end is thicker and the flow rate of the end-induced flow is higher, so the restoring effect is stronger. In addition, the flow injected toward the centerline is bounced back to the outer region, and then bounced to the centerline again on the side wall. This bouncing motion facilitates the ending of the CRZ. At a higher injection angle, the radial momentum of the injected flow is higher, which strengthens the bouncing effect of the injected flow. For these two reasons the CRZ ends before the swirl number decreases to the critical value, and the position of the downstream stagnation point moves upstream at lower Reynolds numbers and higher injection angles.

Figure 7 shows the swirl number at the end of the CRZ for different injection angles and Reynolds numbers. This is equivalent to the critical swirl number S_c in the literature. In this figure S_{end} shifts in the range from 0.58 to 0.79. This range is higher than that of the flows in the chamber with slip head end.[14] For a given injection angle, S_{end} is higher at a lower Reynolds number. At any fixed Reynolds number, S_{end} is higher at a higher injection angle. These trends confirm the conclusion drawn in the above analysis, that the end-induced flow and the injected flow tend to end the CRZ before the swirl number decreases to the critical value, and this effect

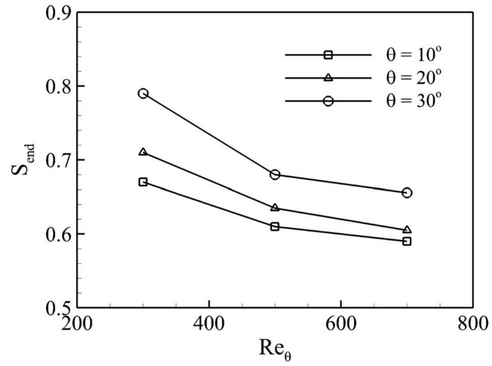

FIG. 7. Dependence of the swirl number at the end of the CRZ on the Reynolds number at different injection angles.

is stronger at a lower Reynolds number and higher injection angle.

The profiles of axial and azimuthal velocities at the end of the CRZ are shown in Fig. 8. To accommodate the discrepancies between injection angles, the velocities in this plot are normalized by the radial component of injection velocity, which is given as $U_{r,in} = U_{\theta,in} \tan\theta_{in}$. As in the flow in the chamber with slip head end, the curves for different Reynolds numbers and injection angles are close to each other, and collapse onto a single curve for both axial and azimuthal velocities. This confirms the conclusion of Wang and Yang[14] that in basic swirling flows the velocity distributions can be described by self-similar solutions.

The axial variation of swirl number at different injection angles and Reynolds numbers is shown in Fig. 9. The swirl number is given in the logarithmic scale in the figure. It has been shown that for the flows in the chamber with slip head end, the curves collapse onto a single curve in the region of the CRZ when the axial coordinate is normalized with the length of the recirculation zone, and in the downstream region curves with a similar injection angle are close to each other.[14] In the present flows, however, the restoring effect of the Coriolis force and the bouncing effect of the injected flow keep the swirl number at the end of the CRZ above the critical value, so the length of the recirculation zone cannot be used as a characteristic scale to normalize the length scale. In this figure,

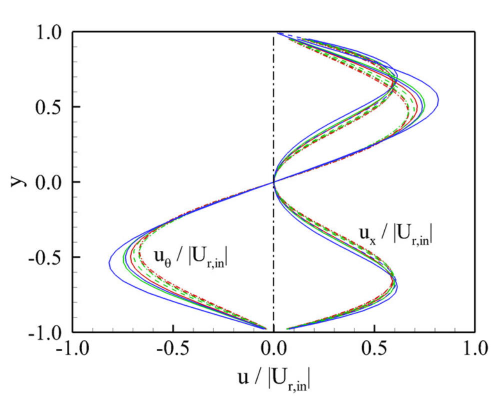

FIG. 8. Distributions of axial and azimuthal velocities at the end of the CRZ. Velocities normalized by radial velocity at the entrance. Red, $\theta_{in} = 10°$; green, 20°; blue, 30°. Solid, $\mathrm{Re}_\theta = 300$; dashed, 500; dashed-dotted, 700.

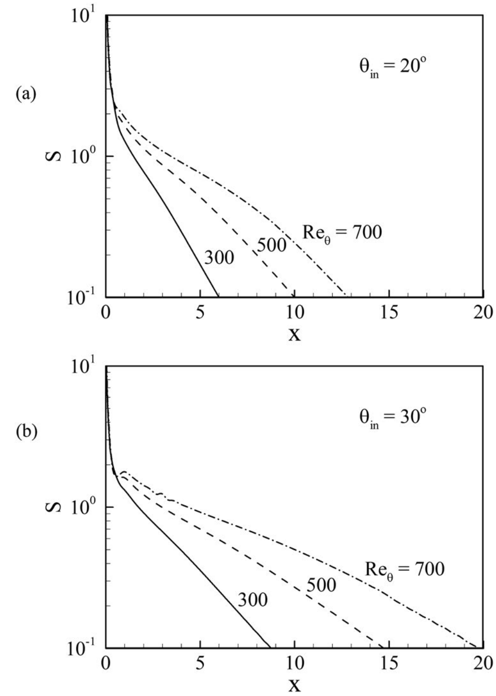

FIG. 9. Variation of the swirl number along the centerline at different injection angles and Reynolds numbers. (a) $\theta_{in} = 20°$; (b) $\theta_{in} = 30°$.

each curve consists of two straight sections corresponding to the CRZ and the downstream region, respectively. The slope in the downstream region is higher than that in the recirculation zone. Since the swirl number is given in the logarithmic scale, we cannot say that the swirl number decreases faster in the downstream region. For a given injection angle, however, the swirl number decreases faster at a lower Reynolds number due to the higher swirl dissipation rate. At any fixed Reynolds number, the swirl number decreases slower at a higher injection angle because of the increase in the flux of angular momentum. At a low Reynolds number, the change of the slope of the curve at the end of the recirculation zone is not obvious. This plot confirms the conclusion that the occurrence of the CRZ is governed by quasi-linear mechanisms.

Compared with the flow in the chamber with the slip head end, the end-induced flow has a suppressing effect on the CRZ. It works like a buffering cushion, enhancing swirl dissipation, and reducing the size of the CRZ. When the Reynolds number is low enough, the CRZ can be entirely wiped out by end-induced flow. Figure 10 shows the flow patterns for different injection angles at $\mathrm{Re}_\theta = 200$. In the flows in the chamber with the slip head end, a CRZ can be observed under the same conditions,[14] but in the presence of a non-slip head end, the end-induced flow is so strong that it completely eliminates the CRZ. Although the streamline patterns look smooth, the free shear layer that is represented by the concentrated vorticity magnitude in the figure has been created by the differences in axial and azimuthal velocities between the outer main flow and the end-induced flow. With an increase in the injection angle, the free shear layer is driven closer to the centerline. At the same time, both the azimuthal velocity and the axial velocity at the outer boundary of the free shear layer increase according to the conservation of angular momentum and the

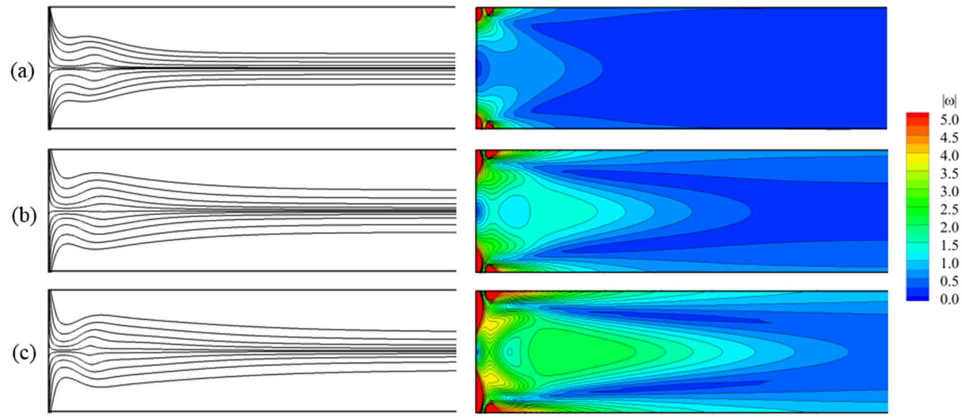

FIG. 10. Projected streamline and vorticity magnitude contours on the x-y plane at Re_θ = 200. (a) θ_{in} = 10°; (b) θ_{in} = 20°; (c) θ_{in} = 30°.

volume flow rate, so the vorticity magnitude in the free shear layer increases correspondingly.

To compare the flow fields quantitatively, we plot the profiles of axial velocity, azimuthal velocity, and vorticity magnitude along the vertical line at x = 0.3, in Fig. 11. As the injection angle increases from θ_{in} = 10° to 30°, the axial and azimuthal velocities increase throughout the field. The peaks of both velocities and vorticity magnitude shift to the centerline as the injection angle increases. From the curves of vorticity magnitude in Fig. 11(c), the free shear layer can be identified by the peaks of vorticity magnitude.

B. Columnar central recirculation zone with instability waves at high swirl level

The basic patterns of the flows with an axisymmetric CRZ demonstrate that a free shear layer is developed at the interface between the outer main flow and the end-induced flow. Via the free shear layer, the outer flow drives the central flows, including the end-induced flow and the central recirculating flow, to take on a solid body rotation. The velocity jump across the free shear layer and the solid-body rotation of the central flows provide the potential for the development of Kelvin-Helmholtz instability waves and inertial waves in the flow, respectively. The instability waves will be triggered when the Reynolds number and injection angle meet the requirements for the development of these waves. In this section, we discuss the instability waves that appear in the flow at high swirl level. The instabilities are initiated by increasing the Reynolds number.

Figure 12 shows instantaneous streamline patterns on the x-y plane for different Reynolds numbers at θ_{in} = 10°. We

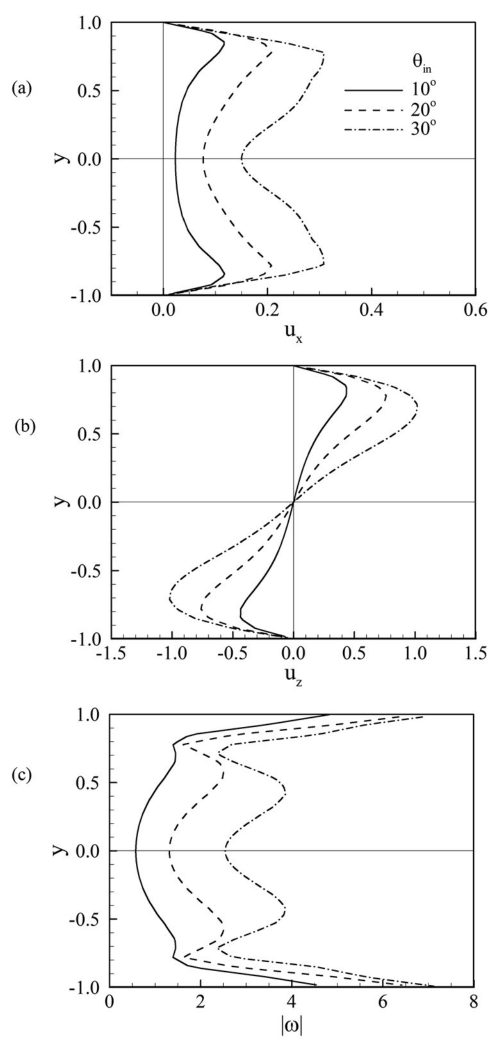

FIG. 11. Profiles of (a) axial velocity, (b) azimuthal velocity, and (c) vorticity magnitude at x = 0.3 in flow without the CRZ at Re_θ = 200.

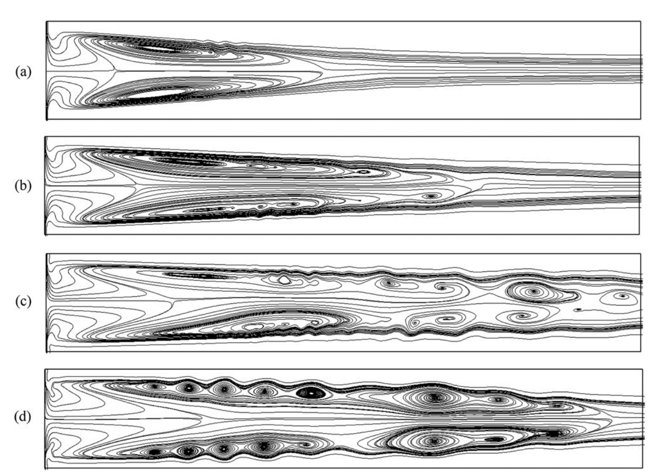

FIG. 12. Instantaneous streamlines projected on the x-y plane at θ_{in} = 10°. (a) Re_θ = 1000; (b) Re_θ = 1500; (c) Re_θ = 2000; (d) Re_θ = 3000.

know from the above discussion that the flow remains stable until Re_θ exceeds 700. At $\mathrm{Re}_\theta = 1000$, small wrinkles appear at the boundaries of the downstream half of the CRZ. As Re_θ increases to 1500, these small wrinkles evolve into modulated recirculation bubbles aligned longitudinally in the CRZ. These small recirculation bubbles become larger when Re_θ increases to 2000. At this point, these small bubbles are still distributed in a relatively random manner. When the Reynolds number increases to 3000, these randomly distributed recirculation bubbles evolve into a highly structured vortex train pattern. In the upstream half of the CRZ, the small recirculation bubbles are aligned along the boundaries of the CRZ. As the flow travels downstream, the bubbles converge to the centerline. This feature implies that in the upstream half of the CRZ, where the free shear layer is strong, the waves are characterized by Kelvin-Helmholtz instability formed as a result of the axial velocity jump across the free shear layer. In the downstream half of the CRZ, the free shear layer is weakened, yet the angular velocity of the central flows increases, which makes the Kelvin-Helmholtz instability waves evolve into inertial waves. In the present condition, the flow patterns remain almost axisymmetric and no azimuthal wave is observed perhaps because the free shear layer is close to the sidewall at low injection angles, and this suppresses the development of azimuthal waves. In addition, the viscous head end also has a damping effect on the azimuthal waves.

In order to better understand the flow characteristics, we select the flow at $\theta_{in} = 10°$ and $\mathrm{Re}_\theta = 3000$ as an example. Figure 13 shows the typical patterns of this flow on the x-y plane. The projected streamlines shown in Fig. 13(a) feature two rows of recirculating bubbles embedded in the CRZ. From the discussion with respect to Fig. 12, the waves in the upstream half of the CRZ are attributed to the axial velocity jump across the free shear layer and therefore can be considered Kelvin-Helmholtz waves. In the downstream half of the CRZ, the angular velocity of the central flows increases sufficiently for the instability waves to switch to inertial waves. The contours of axial velocity are shown in Fig. 13(b). The velocity increment between neighboring contour lines is constant throughout the field, so the density of the contour lines demonstrates the sharpness of the velocity change. This figure shows that in the central region the axial velocity does not change much and remains at a low value. At the boundaries of the central region, the axial velocity changes sharply, and the gradient provides the driving power for the Kelvin-Helmholtz instabilities. Due to the high Reynolds number, the layer of end-induced flow enclosing the CRZ is thin, so the free shear layer is roughly located at the boundary of the CRZ.

The contours of azimuthal velocity are shown in Fig. 13(c). The contour lines in the downstream half of the CRZ converge to the centerline, which implies that the angular velocity of the solid-body rotation is higher in the downstream half and facilitates the development of inertial waves. In the contours of vorticity magnitude shown in Fig. 13(d), the free shear layer, represented by the layer with higher vorticity magnitude enveloping the CRZ, breaks up into a series of small patches with the development of Kelvin-Helmholtz instability waves. In the downstream end of the CRZ, the small recirculating bubbles of the inertial waves cause the convergence of vorticity magnitude on the centerline. All the patterns in Fig. 13 confirm the conclusion arrived at in the analysis of Fig. 12 that the longitudinal waves at high swirl level consist of two parts: Kelvin-Helmholtz waves in the upstream region of the CRZ and inertial waves in the downstream region.

C. Bubble type vortex breakdown at medium swirl level

In the boundary layer on the head end of the chamber, the unbalanced pressure gradient drives the flow to the centerline, which causes a concentration of vorticity magnitude on the centerline. With the increase in the injection angle, the concentrated vorticity magnitude eventually evolves into a vortex core. According to the strict definition, the formation of a preceding vortex core is a prerequisite for the occurrence of vortex breakdown.[9] As noted above, we have found that at high injection angle the outer flow injected toward the centerline is bounced back to the outer region and is then bounced again toward the centerline on the sidewall. At the same time, the Coriolis force in the swirling system gives the flow deviating

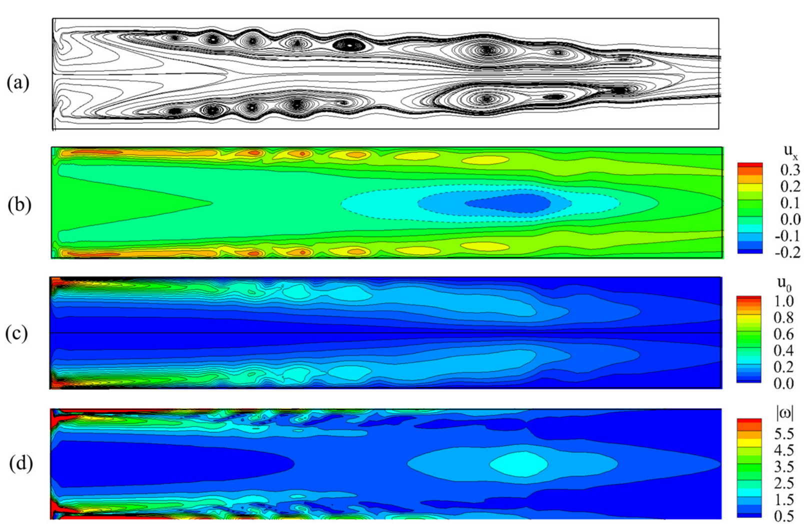

FIG. 13. Flow patterns on the x-y plane of the columnar CRZ with longitudinal waves at $\theta_{in} = 10°$ and $\mathrm{Re}_\theta = 3000$: (a) streamlines; (b) contours of axial velocity; (c) contours of azimuthal velocity; (d) contours of vorticity magnitude.

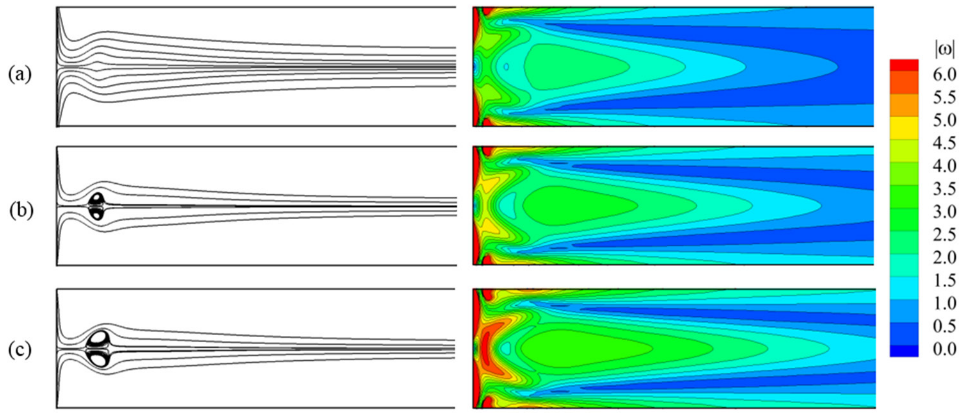

FIG. 14. Projected streamline and contours of vorticity magnitude on the x-y plane at Re_θ = 200. (a) θ_{in} = 30°; (b) θ_{in} = 35°; (c) θ_{in} = 40°.

from the centerline a tendency to return to the centerline. These two effects, together with the formation of the preceding vortex core, facilitate the occurrence of another type of a CRZ, the commonly observed bubble-type vortex breakdown. Compared with the columnar CRZ at high swirl level, bubble-type vortex breakdown is a highly nonlinear phenomenon. Over the years, many experimental and numerical studies have been done in this area.[20,21] It should be noted that bubble-type vortex breakdown cannot take place in a chamber with the slip head end[14] because the injected flow does not converge to the centerline with the slip condition on the head end.

Figure 14 shows the occurrence of bubble type vortex breakdown as the injection angle increases from θ_{in} = 30° to 40° at Re_θ = 200. As shown in Fig. 14(a), no flow recirculation can be observed in the flow at θ_{in} = 30°, but the curvy pattern of the streamlines near the centerline shows the tendency to form a recirculation zone. When θ_{in} increases to 35°, a small bubble-like CRZ appears on the centerline. As θ_{in} further increases to 40°, the bubble appears to grow in size. The contours of vorticity magnitude in Fig. 14 show that a free shear layer is formed between the outer main flow and the end-induced flow. With the increase in the injection angle, the free shear becomes stronger and shifts to the centerline. When θ_{in} increases up to 45°, the free shear layer converges on the centerline and forms a region with concentrated vorticity magnitude before the recirculation zone. This region forms the prototype of the axisymmetric vortex core before vortex breakdown. In the preceding discussion, Figs. 10 and 11 show that at Re_θ = 200 no CRZ is present, due to the damping effect of end-induced flow when $\theta_{in} \leq 30°$. At the same time, Fig. 5(a) indicates that the increase in the injection angle has a suppression effect on the development of the CRZ. This confirms that the CRZ of bubble type vortex breakdown appearing at $\theta_{in} > 30°$ is inherently different from the CRZ driven by centrifugal force at high swirl level and is purely caused by the bouncing of the injected flow and the restoring effect of the Coriolis force.

The flow patterns of a typical bubble type vortex breakdown at θ_{in} = 60° and Re_θ = 200 are shown in Fig. 15. The instantaneous streamline patterns in Fig. 15(a) show that the appearance of the bubble type vortex breakdown is similar

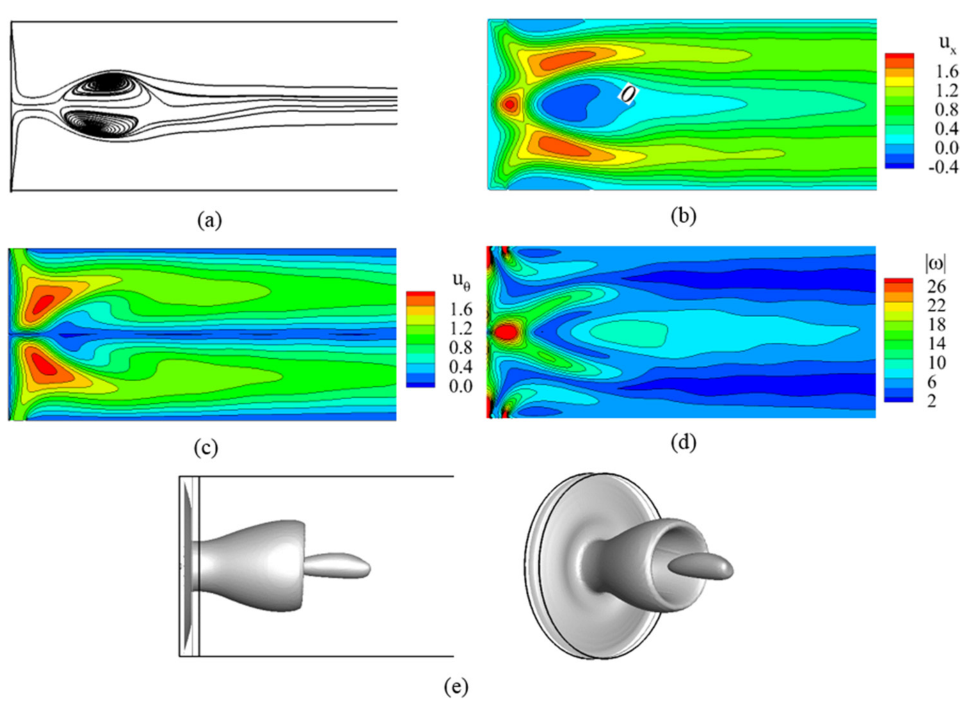

FIG. 15. Overview of bubble type vortex breakdown at θ_{in} = 60° and Re_θ = 200. (a) projected streamlines; (b) contours of axial velocity; (c) contours of azimuthal velocity; (d) contours of vorticity magnitude on the x-y plane; and (e) iso-surfaces of vorticity magnitude, $|\omega|_{iso}$ = 8.

to that of the CRZ driven by centrifugal force, although we have shown, earlier, that the causes of these two phenomena are totally different. The contours of axial velocity on the *x-y* plane are shown in Fig. 15(b). In the outer region, the injected flow travels downstream with larger axial velocity (colored red in the figure). In the central region, a jet flow with higher axial velocity is created on the centerline, followed by the recirculation zone with negative axial velocity. In the flow at a lower injection angle, such as that at θ_{in} = 20° and Re_θ = 300 shown in Fig. 3, this jet flow cannot be observed, due to the smaller flow momentum in the radial direction. Figure 15(c) shows the contours of azimuthal velocity on the *x-y* plane. Between the head end and the central recirculation bubble, the azimuthal velocity is concentrated around the jet flow and decreases monotonically to zero on the centerline inside the jet. With the occurrence of vortex breakdown, the region with high azimuthal velocity expands at the upstream end of the recirculation bubble and extends downstream along the bubble surface. As a result, the azimuthal velocity inside the recirculation bubble is low relative to outside the bubble. This azimuthal velocity distribution is distinct from what we observed in the CRZ driven by centrifugal force, shown in Fig. 3, in which the CRZ, together with the end-induced flow, takes on a solid body rotation. In the downstream half of the bubble of vortex breakdown, the contour lines converge to the centerline and create a long stretch with solid-body rotation in the downstream region. The angular velocity in the downstream region is higher than that inside the bubble, and this facilitates the development of inertial waves in the wake of the vortex breakdown bubble. Figure 15(d) shows the contours of vorticity magnitude on the *x-y* plane. One important characteristic of the vorticity field is the formation of an axisymmetric preceding vortex core on the centerline; this differentiates the bubble type vortex breakdown from the CRZ driven by centrifugal force at high swirl level. As vortex breakdown takes place, the vortex core expands at the stagnation point and forms a bell-shaped vortex layer covering the recirculating bubble. It should be noted that the vortex layer evolves from the preceding vortex core, which mainly consists of the end-induced flow, so the vortex layer is not caused by the velocity difference between the outer and central flows and does not overlap the surface of the recirculating bubble. The corresponding three-dimensional vortex structures are shown in Fig. 15(e), in which an axisymmetric vortex core followed by a bell-like vortex layer is presented. In the rear part of the recirculating bubble, an asymmetric vortex core with weaker strength can be observed on the centerline. This weaker vortex core is created by the convergence of flow to the centerline at the downstream end of the recirculating bubble.

The profiles of axial velocity are shown in Fig. 16(a). The curves show a central peak with higher magnitude, corresponding to the jet flow of the vortex core, and two side peaks correspond to the outer main flow injected into the chamber. With an increase in the injection angle, all the peak values increase. For bubble type vortex breakdown, which generally occurs at a low Reynolds number, the strength of the preceding vortex core is strongly influenced by the injection angle. Figure 16 shows the distributions of axial velocity, azimuthal velocity, and vorticity magnitude of the preceding vortex core at different injection angles from 45° to 75° at the position

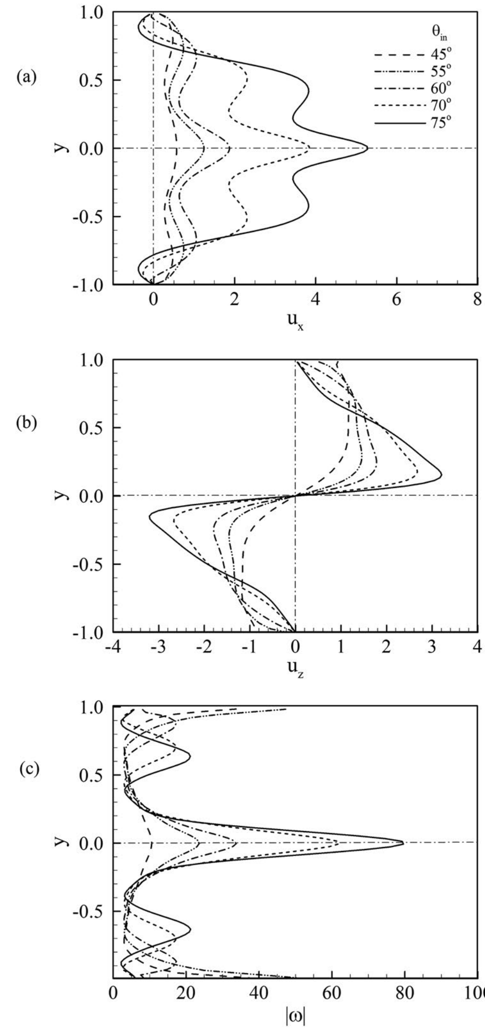

FIG. 16. Profiles of (a) axial velocity, (b) azimuthal velocity, and (c) vorticity magnitude of the preceding vortex core at Re_θ = 200.

where the maximum axial velocity is obtained on the centerline. In Fig. 16(b), we use u_z instead of u_θ to demonstrate the smooth transition of azimuthal velocity on the centerline. As shown in Fig. 16(b), the azimuthal velocity varies inversely with the radial coordinate in the outer region and reaches a peak outside the vortex core. This implies that in the upstream region the azimuthal velocity is still partially subject to the conservation of angular momentum in the presence of the non-slip condition on the head end. In the central region occupied by the vortex core, the azimuthal velocity changes roughly linearly with the radial coordinate, which implies that the preceding vortex core takes on a solid-body rotation before breakdown. The comparison of these curves shows that the peak value increases as the injection angle increases. At the same time, the curve peak shifts closer to the centerline. It has been found that the profile of the azimuthal velocity of the vortex core is similar to that of the well-known Burgers' vortex.[22] Figure 16(c) shows the profiles of vorticity magnitude. The central peak demonstrates the presence of the central vortex core; the peak value is larger at a higher injection angle. From these curves, the influences of the injection angle on the vortex core can be summarized as follows: the increase in the injection angle decreases the radius of the vortex core, while it

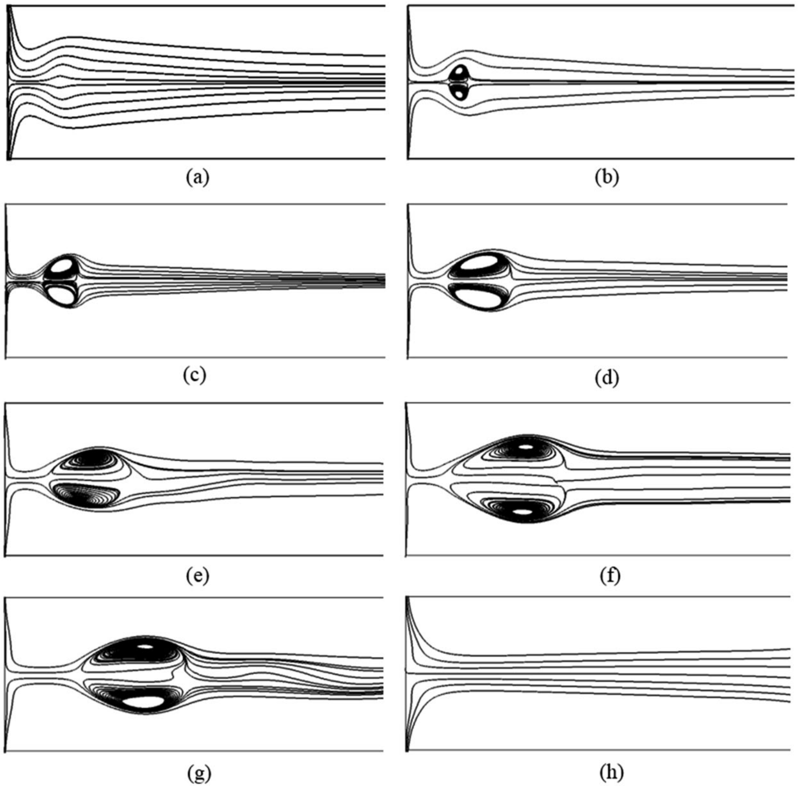

FIG. 17. Projected streamlines on the x-y plane of bubble-type vortex breakdown at $\mathrm{Re}_\theta = 200$. (a) $\theta_{in} = 30°$; (b) $\theta_{in} = 35°$; (c) $\theta_{in} = 45°$; (d) $\theta_{in} = 55°$; (e) $\theta_{in} = 60°$; (f) $\theta_{in} = 65°$; (g) $\theta_{in} = 70°$; (h) $\theta_{in} = 75°$.

increases the azimuthal velocity, axial velocity, and vorticity magnitude inside the vortex core. That is, the vortex core is stronger at a higher injection angle.

Figure 17 shows the streamline patterns of bubble type vortex breakdown at different injection angles. The Reynolds number is fixed at $\mathrm{Re}_\theta = 200$. Before the injection angle increases to $\theta_{in} = 65°$, the bubble size increases monotonically with the injection angle, and the upstream stagnation point remains roughly fixed on the centerline. After $\theta_{in} = 65°$, further increase in the injection angle makes the effect of the increased mass flow rate dominant, which not only squeezes the bubble size but also drives the bubble downstream. At $\theta_{in} = 75°$, the bubble is completely wiped out, and the streamlines only curve slightly, far downstream.

The injection angle influences the recirculating bubble in several ways. First, the injection angle determines the strength of the preceding vortex core, which provides the prerequisite for the occurrence of vortex breakdown. In general, the vortex core is stronger at a higher injection angle, which creates a larger recirculating bubble. Second, the bouncing effects of the injection, together with the restoring effect of the Coriolis force, provide another important impetus for vortex breakdown. At a higher injection angle, the radial component of flow momentum is larger, and this facilitates the increase in bubble size. However, an increase in the injection angle increases the volume flow rate injected into the chamber, which tends to squeeze the size of the recirculating bubble and drives the bubble downstream. That is why the bubble size decreases and the bubble moves downstream after $\theta_{in} = 65°$. The behaviors of bubble type vortex breakdown are the consequence of the competition among these three effects. At lower injection angles, the first two effects dominate the effect of the volume flow rate, and at higher injection angles, the effect of the increased volume flow rate becomes dominant.

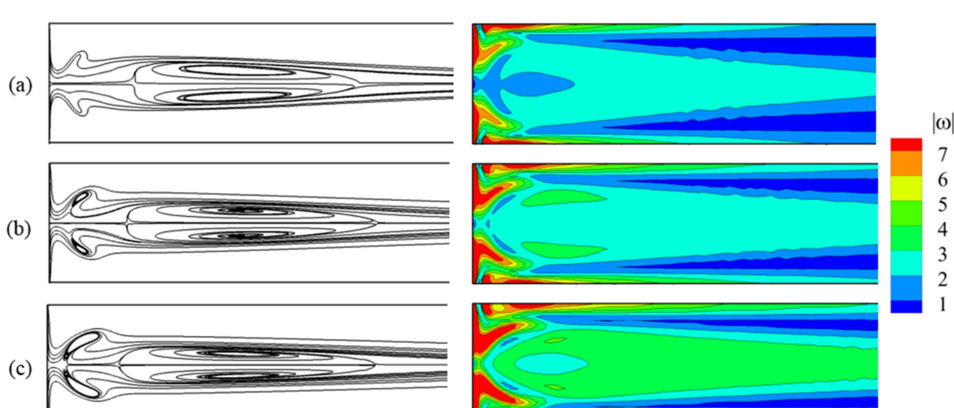

FIG. 18. Flow patterns of bubble-type vortex breakdown with the columnar CRZ at $\mathrm{Re}_\theta = 500$. (Left) Projected streamlines on the x-y plane and (right) vorticity magnitude contours. (a) $\theta_{in} = 30°$; (b) $\theta_{in} = 35°$; (c) $\theta_{in} = 40°$.

In the earlier discussion of bubble type vortex breakdown, we restricted the Reynolds number to the low range (Re_θ = 200), where the columnar CRZ driven by centrifugal force is completely eliminated by the end-induced flow. However, if the Reynolds number is raised to an appropriate higher level, the bubble type vortex breakdown can coexist with the centrifugal-force-driven columnar CRZ. Figure 18 demonstrates the process of creating a bubble type vortex breakdown in the flow with a columnar CRZ by increasing the injection angle from $\theta_{in} = 30°$ to 50°. The Reynolds number is fixed at $Re_\theta = 500$, where the flow is characterized by a columnar CRZ at high swirl level. At $\theta_{in} = 30°$, the recirculating bubble of vortex breakdown has not been created, but the curvy pattern of the streamlines in the upstream region of the columnar CRZ shows a tendency toward vortex breakdown. When the injection angle is increased to $\theta_{in} = 35°$, an annular recirculating bubble is created in the upstream region, which indicates that bubble type vortex breakdown is taking place. When the injection angle is further increased to $\theta_{in} = 40°$, the bubble size increases significantly.

It is known that the columnar recirculation zone only appears when the swirl number exceeds a critical value,[14] and its longitudinal length explicitly depends on the swirl dissipation rate, so the columnar recirculation zone extends to a considerable length in these flows. Yet the bubble type vortex breakdown is created by the bouncing effect of the injected flow and the restoring effect of the Coriolis force, so the aspect ratio of the bubble is always around one, and the swirl number is not required to be small at the end of the recirculation bubble. Thus as shown in this figure, the vortex breakdown bubbles are all in the upstream region, where the swirl number is much higher than the critical value. The contours of vorticity magnitude show that the vortex breakdown bubble is enclosed by the free shear layer. With the increase in the injection angle, the free shear layer moves toward the centerline, and the vortex magnitude in the layer eventually becomes larger. This is consistent with what we observed at $Re_\theta = 200$ in Fig. 14.

The typical flow patterns at $Re_\theta = 500$ and $\theta_{in} = 40°$ are used as an example to illustrate the characteristics of bubble-type vortex breakdown with columnar CRZ in Fig. 19. The streamline patterns feature a transversely expanding recirculation bubble followed by a longitudinally elongated recirculation zone, as shown in Fig. 19(a). The contours of axial velocity in Fig. 19(b) show that the outer main flow passes outside the two recirculation zones with higher velocity. In the central region, inside the recirculation zones, the velocity magnitude is much lower than that in the outer region. The contours of azimuthal velocity in Fig. 19(c) show that the recirculation bubble of vortex breakdown does not take on solid-body rotation like the columnar CRZ in the downstream. The transverse expansion of the contour lines in the region of the vortex breakdown bubble implies that the azimuthal velocity of the vortex breakdown bubble is lower than that of the columnar CRZ downstream. As in the flow without the columnar recirculation zone shown in Fig. 15, an obvious convergence of contour lines to the centerline can be observed in the downstream half of the vortex breakdown bubble, which enhances the possibility of the development of inertial waves in the downstream region occupied by the columnar CRZ. The corresponding contours of vorticity magnitude are shown in Fig. 19(d), which demonstrates the lateral expansion of the free shear layer due to the occurrence of vortex breakdown. In the downstream region, the columnar CRZ does not induce any visible disturbances in the vorticity field. This is primarily because the CRZ has only passive motion, as discussed in Sec. IV A.

The above analysis of the flow patterns demonstrates that bubble type vortex breakdown is inherently distinct from the columnar CRZ driven by centrifugal force. The differences can be summarized as follows. The columnar CRZ is a quasi-linear phenomenon, which is created by strong centrifugal force at high swirl level. It only appears when the swirl number exceeds a critical value. The central recirculating flow takes on a passive solid-body rotation, which is driven by the outer main flow through the free shear layer. The bubble type vortex breakdown is a nonlinear phenomenon, which is created by the bouncing effect of the injected flow and the restoring effect of the Coriolis force in the swirling system. The occurrence of bubble type vortex breakdown does not explicitly depend on the swirl number. The recirculating bubble is not in solid-body rotation and remains at a low swirl level. The bouncing and restoring effects keep the aspect ratio of the bubble at around one. One major characteristic of bubble type vortex breakdown is the formation of a preceding central vortex core, which expands at the upstream stagnation point of the recirculating bubble to form a bell-shaped free shear layer.

D. Columnar central recirculation zone (CRZ) with instability waves at medium swirl level

In Secs. IV A–IV C, we have found that the flow behaviors are completely determined by the injection angle and Reynolds number. At high swirl level ($\theta_{in} \leq 30°$), the flow is dominated by the centrifugal force, and in the lower Reynolds number

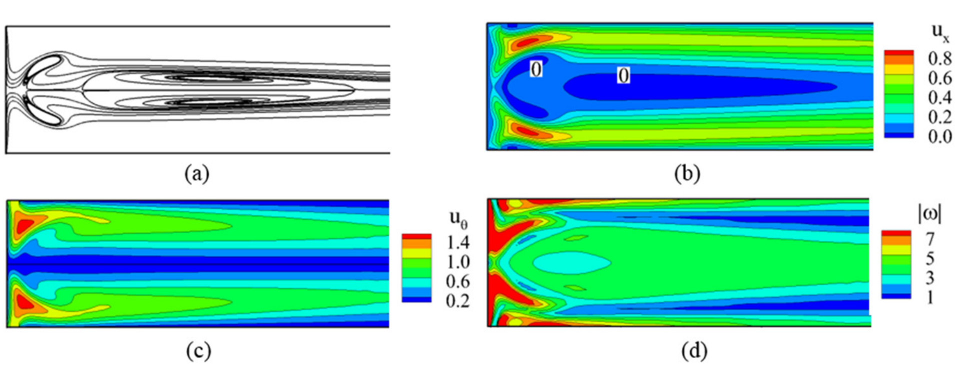

FIG. 19. Flow patterns on the x-y plane of bubble-type vortex breakdown with the columnar CRZ at $Re_\theta = 500$ and $\theta_{in} = 40°$: (a) projected streamlines; (b) contours of axial velocity; (c) contours of azimuthal velocity; (d) contours of vorticity magnitude.

range ($\mathrm{Re}_\theta < 1000$), it is characterized by a columnar CRZ. When the Reynolds number exceeds 1000, the flow becomes unstable, and longitudinal Kelvin-Helmholtz instability waves and inertial waves develop in the flow. In this range of the injection angle, the azimuthal propagating waves are suppressed by the viscous dissipation on the side wall. With an increase in the injection angle, the free shear layer between the outer and central flows shifts to the centerline, which reduces the suppression effect of the side wall and facilitates the development of azimuthal Kelvin-Helmholtz waves. At the same time, the bouncing effect of the injected flow and the restoring effect of the Coriolis force are strengthened, and this creates bubble-type vortex breakdown when $\mathrm{Re}_\theta < 500$. The recirculating bubble is enclosed by the free shear layer. When the Reynolds number goes beyond a critical value related to the injection angle, the free shear layer becomes unstable and azimuthal Kelvin-Helmholtz instability waves develop. Compared with the waves in the chamber with slip head end,[14] the unbalanced radial pressure gradient in the boundary layer on the head end drives the free shear layer closer to the centerline and decreases its perimeter. At the same time, the boundary layer on the head end smears the sharpness of the free shear layer. Both of these processes tend to damp the waves and decrease the azimuthal wave number.

Here we use the flow at $\theta_{in} = 45°$ and $\mathrm{Re}_\theta = 500$ as an example to analyze the flow characteristics with instability waves. An overview of the flow patterns is given in Fig. 20. The cross section $x = 0.1$ is located in the region strongly influenced by the surface friction on head end, and $x = 0.5$ is located where the instability waves fully develop. As shown in Fig. 20(a), the axisymmetric free shear layer rolls up into three discrete vortex cores aligning uniformly in a circle at the head end; that is, the dominant azimuthal wave number is $m = 3$. In the quasi-steady state, the flow structures are time independent and rotate on the centerline with a constant precession frequency. It was found that for the flow under the same conditions in the chamber with the slip head end[14] the azimuthal waves are dominated by the $m = 4$ mode in the upstream region. This reduction of wave number confirms the conclusion that the nonslip condition on the head end has a damping effect on the wave number. In the cross sections, three vortex cores with concentrated vorticity magnitude can be observed. Due to the unbalanced pressure gradient in the boundary layer on the head end, the vortex cores are closer to the centerline at $x = 0.1$ than at x = 0.5. At the same time, the damping effect of the boundary layer keeps the vorticity magnitude inside the vortex core at $x = 0.1$ lower than that at $x = 0.5$. The contours on the x-y plane indicate that the instability waves attenuate eventually as flow travels downstream, and the vortex cores only exist in a limited region upstream.

Figure 20(b) shows the typical three-dimensional streamlines around one vortex core and the projected streamlines on the cross sections $x = 0.1, 0.5$, and the longitudinal central plane $z = 0$. The streamlines are made with the velocity components in the frame rotating with the flow structures, so they coincide with the trajectories of the fluid particles in the rotating frame. The streamlines around each vortex core rotate about the core centerline and travel downstream along the spiral vortex core. On the planes $x = 0.5$ and $z = 0$, the instability waves appear as a series of eye-like recirculating bubbles in the projected streamlines. At $x = 0.1$, the instability waves are weak, so the eye-like bubbles cannot be observed on the cross section.

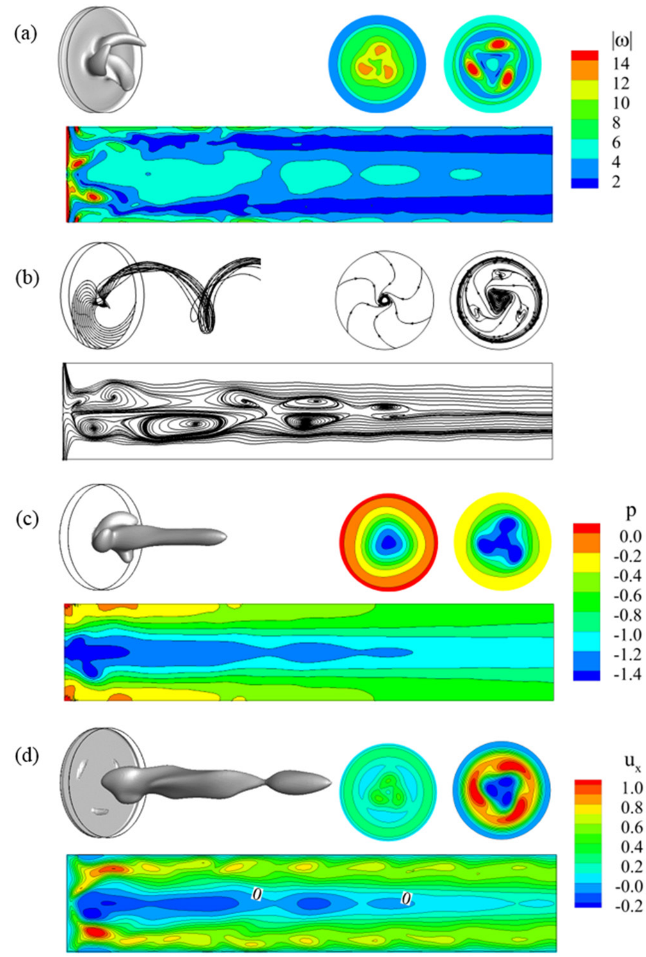

FIG. 20. Patterns of the CRZ with instability waves at $\theta_{in} = 45°$ and $\mathrm{Re}_\theta = 500$. Contours at cross sections x = 0.1 and 0.5 and central plane z = 0. (a) vorticity magnitude, $|\omega|_{iso} = 10$; (b) streamlines; (c) pressure, $p_{iso} = -1.2$; (d) axial velocity, $(u_x)_{iso} = 0$.

Because of the sharp turning motion of the fluid particles around the vortex cores, three low-pressure cores are created along the vortex cores, as shown in Fig. 20(c). The low-pressure core on the centerline is caused by the swirl motion of the bulk flow. At $x = 0.1$, low-pressure cores have not developed. The pressure contours show a trend that decreases monotonically toward the centerline. At $x = 0.5$, with the strengthening of the instability waves, three low pressure cores can be observed at the wave "eyes." Like the vortex cores, the pressure contours on the x-y plane indicate that the low-pressure cores do not extend far in the downstream direction.

Figure 20(d) gives the patterns of axial velocity u_x. The iso-surface at $u_x = 0$ shows the surfaces of the central flow reversal zone defined as the region in which $u_x < 0$. Because of the instability waves, the flow reversal zone twists in the upstream region. At $x = 0.1$, the axial velocity is not fully developed and the surface friction on the head end suppresses the instability waves, so the axial velocity is smaller than that at $x = 0.5$. The flow in the outer region, which has just been injected into the chamber, stays axisymmetric, and the

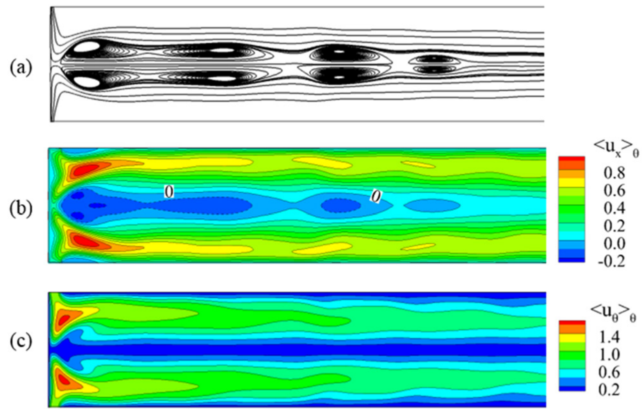

FIG. 21. Flow patterns based on the azimuthally averaged flow field at θ_{in} = 45° and Re_θ = 500. (a) Projected streamlines on the *x-y* plane; (b) contours of axial velocity $\langle u_x \rangle_\theta$ on the *x-y* plane; (c) contours of azimuthal velocity $\langle u_\theta \rangle_\theta$ on the *x-y* plane.

end-induced flow in the central region decomposes into three branches. At $x = 0.5$, the end-induced flow expands to the outer region and combines and forms modulated patterns with the outer flow. In the central region, the CRZ forms a triplet structure. The contours on $z = 0$ show a deformed flow reversal zone with $u_x < 0$. In the outer region, the axial velocity is larger, which indicates the passage through which most of the injected flow convects downstream. In this situation, the deformed CRZ is no longer closed and mass transfer with the outer flow takes place.

The surfaces of the flow reversal zone [Fig. 20(d)] show that in the downstream region the spiral patterns eventually attenuate, and the modular patterns become axisymmetric. This is because, as the flow travels downstream, the shear strength is weakened through viscous dissipation, the portion of the waves related to Kelvin-Helmholtz instabilities is restricted, and the inertial waves caused by the solid-body rotation of the central flows become dominant. The same phenomenon was observed in the chamber with the slip head end.[14]

Spatial averaging in the azimuthal direction can help us to separate the longitudinal waves from the azimuthal. Figure 21 shows the flow patterns based on the azimuthally averaged flow field. The azimuthally averaged velocities are denoted by $\langle u \rangle_\theta$. The longitudinally aligned recirculation bubbles shown by the streamlines in Fig. 21(a), as well as the modulated patterns in the contours of axial and azimuthal velocities in Figs. 21(b) and 21(c), illustrate the longitudinal waves developing in the flow. The leading bubble is related to the bouncing effect of the injected flow and the restoring effect of the Coriolis force, which was discussed earlier. The leading bubble causes the convergence of azimuthal velocity to the centerline, as shown in Fig. 21(c), and triggers the inertial waves on the centerline. At the same time, the axial velocity change across the free shear layer between the outer and central flows creates the longitudinal Kelvin-Helmholtz waves. Under the present conditions, the Kelvin-Helmholtz waves are so weak that they can hardly be observed in this figure.

The patterns of the perturbation velocity components, u'_x, u'_r, and u'_θ, are shown in Fig. 22. The perturbation velocities are obtained by subtracting the azimuthally averaged velocities from the instantaneous velocities $u' = u - \langle u \rangle_\theta$. Due to the damping effect of the boundary layer on the head end, the magnitudes of all the perturbation velocities are much smaller at $x = 0.1$ than at $x = 0.5$. In the downstream region, the perturbations eventually become weaker due to viscous diffusion and dissipation.

For a given configuration, the behaviors of the instability waves are determined by the Reynolds number Re_θ and the injection angle θ_{in}. In this analysis, mode $m = 1$ is defined as a single asymmetric vortex core and mode $m = 0$ as an axisymmetric vortex core on the centerline. Figure 23 shows the influence of the Reynolds number on the vortex patterns at $\theta_{in} = 45°$. The left column gives the three-dimensional iso-surfaces of vortex magnitude, and the right two columns give the contours of vorticity magnitude on cross sections $x = 0.1$ and 0.5, respectively. $x = 0.1$ is located in the region strongly influenced by the surface friction on the head end, and $x = 0.5$ is located where the instability waves fully develop. In order to show the vortex structures clearly, the levels of iso-surfaces and the scales of contour lines are different for each case. For each case, the contour scales are fixed.

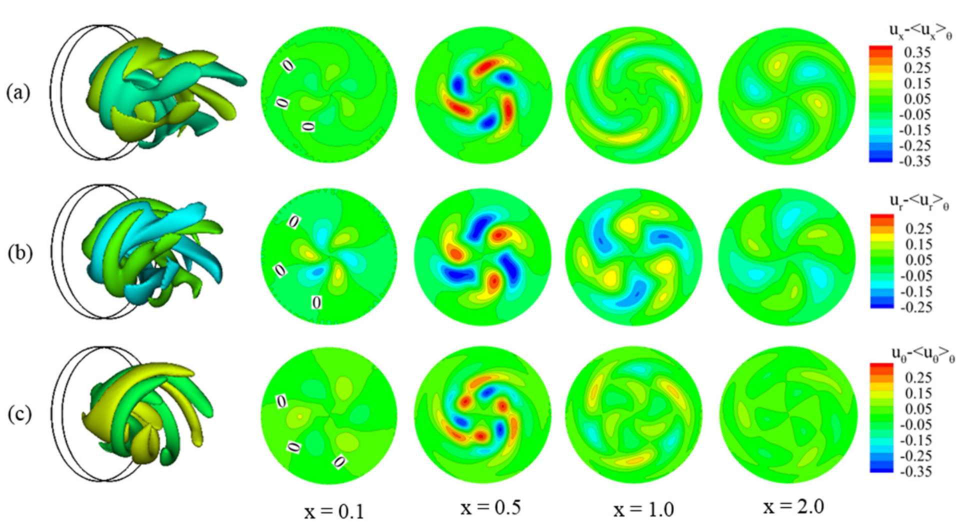

FIG. 22. Patterns of perturbation velocity components at θ_{in} = 45° and Re_θ = 500. (Left) Iso-surfaces of perturbation velocity components and (right four columns) contours of perturbation velocity components at cross sections x = 0.1, 0.5, 1.0, and 2.0. (a) $u_x - \langle u_x \rangle_\theta$; (b) $u_r - \langle u_r \rangle_\theta$; (c) $u_\theta - \langle u_\theta \rangle_\theta$.

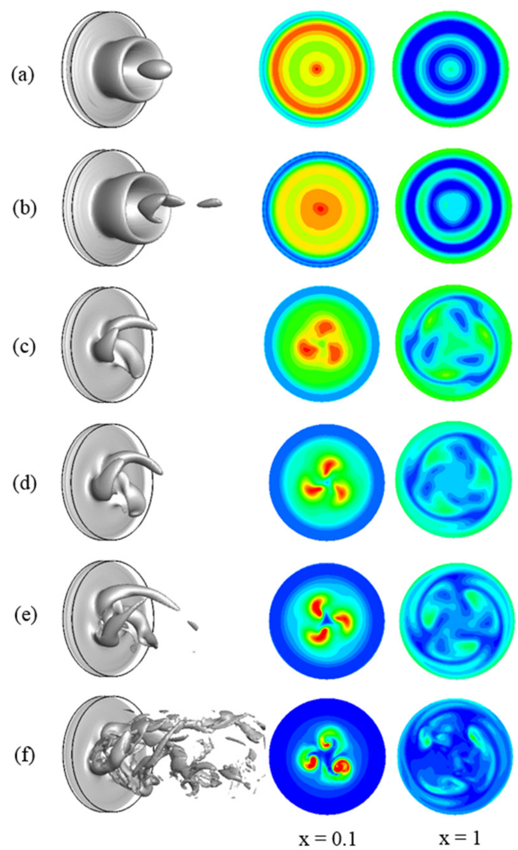

FIG. 23. Vortex structure of instability waves at θ_{in} = 45°. (a) Re_θ = 200; (b) Re_θ = 300; (c) Re_θ = 500; (d) Re_θ = 700; (e) Re_θ = 1000; (f) Re_θ = 2000. The iso-surface level and color scale are different for each case.

At Re_θ = 200, the thicker boundary layer on the head end, in which the unbalanced radial pressure gradient drives the fluid toward the centerline, creates an axisymmetric vortex core on the centerline (m = 0), which can be observed in the contours at x = 0.1. It should be pointed out that the circle with higher vorticity magnitude at x = 0.1 in the figure is created by the surface friction at the entrance rim and has nothing to do with the free shear layer generated on the head end [see Fig. 15(d) for the detailed patterns]. As a result of the bouncing effect of the injected flow and the restoring effect of the Coriolis force, the vortex core expands from the centerline and undergoes bubble-type vortex breakdown. This kind of flow is discussed in Sec. IV C. The circle with higher vorticity magnitude in the contours at x = 0.5 represents the bell-shaped vortex layer of the bubble vortex breakdown.

When the Reynolds number increases to 300, the flow becomes unstable. The preceding vortex core loses symmetry (m = 1), and the free shear layer after breakdown exhibits some features of the azimuthal wave with m = 3. When the Reynolds number increases to 500, the preceding vortex core, together with the free shear layer, breaks up into three discrete vortex cores. Azimuthal Kelvin-Helmholtz instability waves with m = 3 are triggered. Since the preceding vortex core has broken up into three, this flow can no longer be considered to be in vortex breakdown. Strictly speaking, vortex breakdown only refers to the sudden change of an axisymmetric vortex core. At this injection angle θ_{in} = 45°, further increase in the Reynolds number up to Re_θ = 2000 does not lead to an increase in the wave number but rather makes the flow unstable and causes it to develop some fine structures. This is consistent with observations on the chamber with slip head end.[14]

We know that the azimuthal instability waves are caused by the azimuthal velocity change across the free shear layer and are triggered at the place where the flow parameters, such as the flow shear rate and the perimeter of the free shear layer, meet the criterion for the instabilities to occur. At the same time, the nonslip condition on the head end has a suppression effect on wave development. As a result of this, the azimuthal wave number near the head end may be smaller than that at a distance away from the head end.

This wave mode change caused by the head end can be observed at θ_{in} = 55°, as shown in Fig. 24. At Re_θ = 200, a bubble type vortex breakdown is presented. The wave mode stays at $m = 0$. As Re_θ increases to 300, the free shear layer after breakdown splits into two symmetric vortex cores with the development of wave $m = 2$. The preceding vortex core remains axisymmetric ($m = 0$). At $\mathrm{Re}_\theta = 500$, the preceding vortex core loses symmetry and deviates from the centerline. The wave mode of the vortex core becomes $m = 1$. The downstream wave remains at $m = 2$. As Re_θ increases from 500 to 700, the degree of asymmetry of the preceding vortex core increases. At Re_θ = 1000, the preceding vortex core breaks up into two minor vortex cores and connects with the vortex cores downstream.

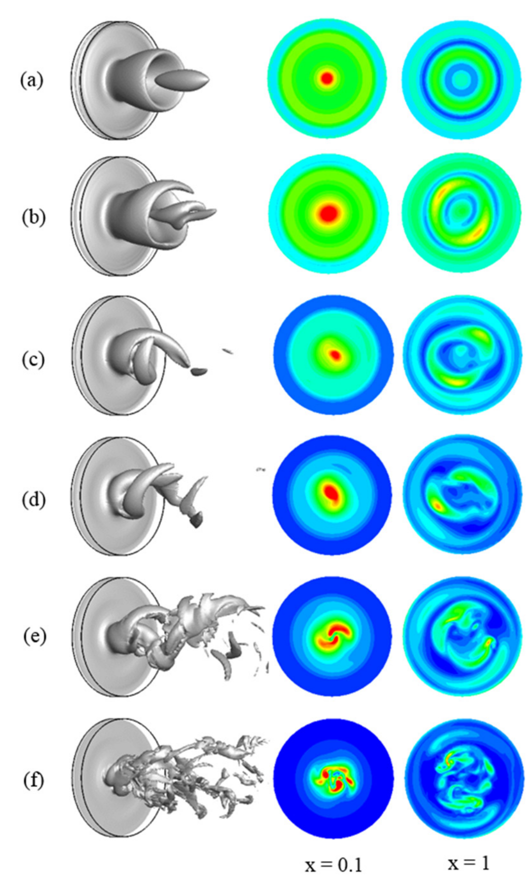

FIG. 24. Vortex structure of instability waves at θ_{in} = 55°. (a) Re_θ = 200; (b) Re_θ = 300; (c) Re_θ = 500; (d) Re_θ = 700; (e) Re_θ = 1000; (f) Re_θ = 2000. The iso-surface level and color scale are different for each case.

At this point, the flow is fully dominated by the azimuthal wave $m = 2$. After that, the wave number does not change with the Reynolds number, up to $Re_\theta = 2000$.

A comparison of Figs. 23 and 24 indicates that the increase in the Reynolds number tends to increase the wave number in both the preceding vortex cores and the downstream free shear layer. Due to the suppression effect of the head end, the wave number in the preceding vortex cores is always equal to or smaller than that in the free shear layer.

The influence of the injection angle on the wave patterns is shown in Fig. 25, which presents three-dimensional iso-surfaces of vorticity magnitude and vorticity contours on the cross sections $x = 0.1$ and 1 for different injection angles at $Re_\theta = 1000$. As the injection angle increases from 30° to 75°, the wave number in the preceding vortex cores decreases from $m = 4$ to 0, and the wave number in the downstream free shear layer decreases from $m = 4$ to 1. At $\theta_{in} = 75°$, an axisymmetric vortex core is created on the centerline, which corresponds to the wave mode $m = 0$. At the upstream stagnation point of the CRZ, the preceding vortex core deviates sharply from the centerline and goes to $m = 1$ on the surface of the CRZ. This phenomenon is characteristic of the spiral type vortex breakdown commonly observed in the flows over delta wings at high angles of attack. The variation of the wave number shown in this figure suggests that the increase in the injection angle tends to decrease the azimuthal wave number in both the preceding vortex cores and the downstream free shear layer. However, at a higher Reynolds number, mode $m = 0$, which corresponds to an axisymmetric vortex core, is hard to reach in the downstream region. In addition, it is found in the simulation that an increase in the injection angle tends to give more random features to the motions of the vortex cores. The stagnation point shifts back and forth on the centerline randomly, the downstream vortex cores lose periodic spiral shape and deform in a random manner, and the whole structure rotates about the centerline with an uneven frequency. All these phenomena suggest that the increase in the injection angle induces nonlinear mechanisms in the flow, and the degree of nonlinearity increases with the injection angle.

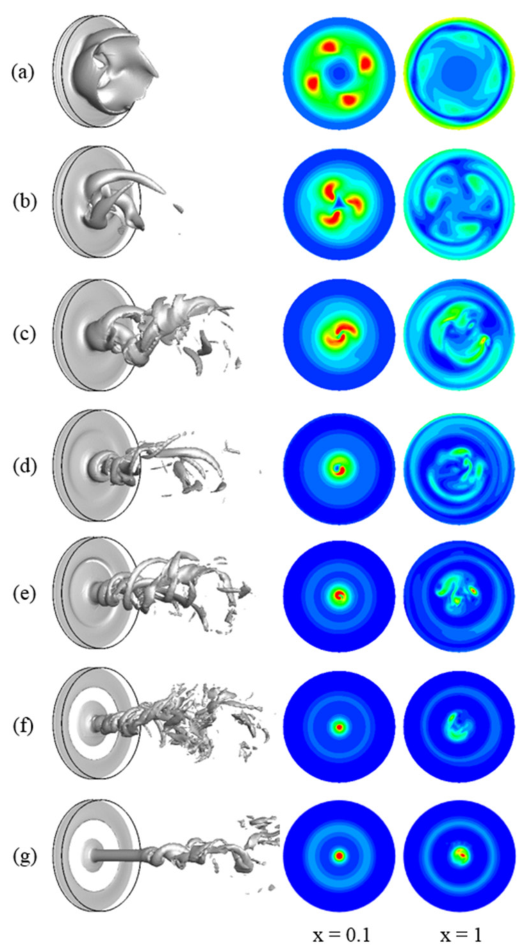

FIG. 25. Influence of the injection angle on the vortex structure of instability waves at $Re_\theta = 1000$. (a) $\theta_{in} = 30°$; (b) $\theta_{in} = 45°$; (c) $\theta_{in} = 55°$; (d) $\theta_{in} = 60°$; (e) $\theta_{in} = 65°$; (f) $\theta_{in} = 70°$; (g) $\theta_{in} = 75°$. The iso-surface level and color scale are different for each case.

E. Spiral type vortex breakdown at low swirl level

As a limiting case of the columnar CRZ with instability waves at high injection angle, spiral vortex breakdown has been the subject of considerable interest.[5,9] In this section, we will briefly discuss the characteristics of spiral vortex breakdown and how it is influenced by the Reynolds number.

Figure 26 gives an overview of the flow patterns of a spiral type vortex breakdown at $\theta_{in} = 75°$ and $Re_\theta = 500$. From the instantaneous streamlines projected on the x-y plane, the spiral vortex breakdown appears as a stagnation point on the centerline, followed by a series of small recirculation bubbles downstream. The small recirculation bubbles are caused by the projection of the three-dimensional streamlines around the

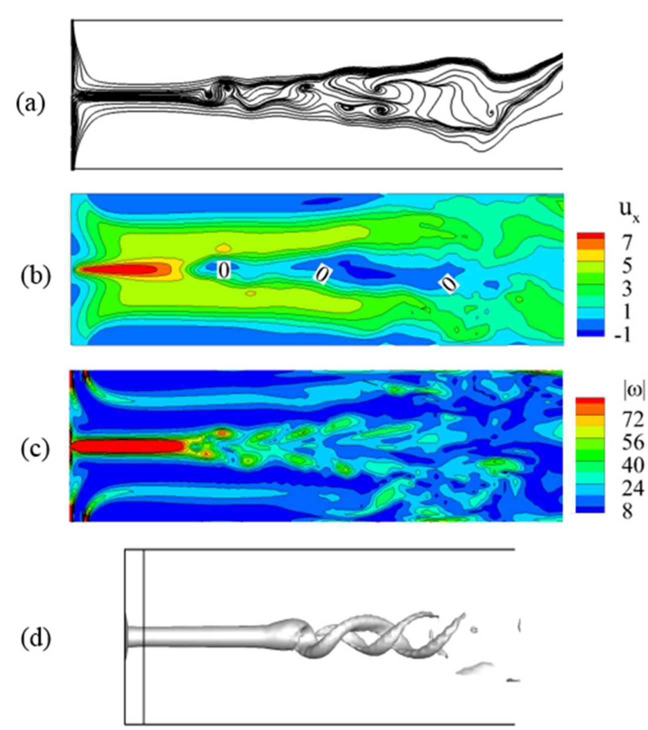

FIG. 26. Overview of spiral type vortex breakdown at $\theta_{in} = 75°$ and $Re_\theta = 500$. (a) Projected streamlines on the x-y plane; (b) contours of axial velocity on the x-y plane; (c) contours of vorticity magnitude on the x-y plane; (d) iso-surfaces of vorticity magnitude, $|\omega|_{iso} = 40$.

spiral vortex core on the x-y plane, and the centers of the bubbles indicate the points where the vortex core passes through the plane.

Figure 26(b) shows the contours of axial velocity on the x-y plane. In the approaching flow, the axial velocity of the vortex core is characterized by a jet-like distribution. At the stagnation point, the jet flow decelerates sharply and goes around the CRZ. In the contours of axial velocity, it is easier to identify the central reversal zone, in which $u_x < 0$, than the CRZ, so we use the central reversal zone in the following discussion.

Due to the interaction with the spiral vortex core after breakdown, the large flow reversal zone disintegrates into several small reversal zones. The vortex patterns are shown in Figs. 26(c) and 26(d), which include the contours on the x-y plane and the three-dimensional iso-surfaces of vorticity magnitude. Before breakdown, an axisymmetric vortex core with concentrated vorticity magnitude is created on the centerline. With the occurrence of vortex breakdown, the straight vortex core deviates from the centerline and extends downstream in a spiral path. It is interesting that another spiral vortex core can be observed with the primary one in the three-dimensional structures. In fact, the minor core does not originate from the preceding vortex core. Instead, it is caused by the spiral structure of the primary vortex core, which inherently tends to attract the outer flow to the central region and thus creates the minor vortex core. (We note that in most of the experiments reported in the literature, the experimental fluid is only dyed in the preceding vortex core, so the minor vortex core cannot be observed.)

A straight vortex core ($m = 0$) is formed on the centerline only when the injection angle is increased to a sufficiently high level. The flow variables in the vortex core, on the other hand, such as axial velocity and vorticity magnitude, are also influenced by the Reynolds number. Figure 27 shows the distributions of axial velocity and vorticity magnitude along the centerline in the vortex core at different Reynolds numbers from 200 to 1000. At $Re_\theta = 200$, the Reynolds number is so low that vortex breakdown does not take place. Only an axisymmetric vortex core appears in the flow. For all cases, neither the axial velocity nor the vorticity magnitude is constant along the centerline. The variation of axial velocity shows a plateau between the head end and the upstream stagnation point of vortex breakdown, which represents the preceding axisymmetric vortex core. The comparison of these curves indicates that at a higher Reynolds number the length of the vortex core is shorter and the axial velocity in the vortex core is larger. Behind the plateau, the axial velocity drops sharply and goes to 0 at the stagnation point. The slope of the curve in the area of rapid decrease is larger at a higher Reynolds number. The curves of vorticity magnitude increase sharply and reach their peaks a small distance from the head end, and then drop monotonically to the stagnation point, where vortex breakdown occurs. With the increase in the Reynolds number, the mean value of vorticity magnitude in the vortex core increases correspondingly. A comparison of the length of the preceding vortex core implies that the vortex core with larger axial velocity and larger vorticity magnitude facilitates the occurrence of vortex breakdown.

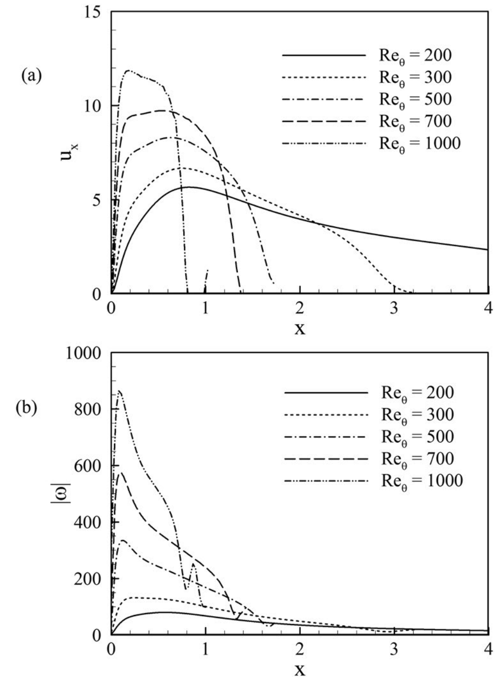

FIG. 27. Variation of (a) axial velocity and (b) vorticity magnitude on the centerline in the preceding vortex core of spiral vortex cores at $\theta_{in} = 75°$.

Figure 28 shows a comparison of the vortex structures of spiral vortex breakdown at different Reynolds numbers. The

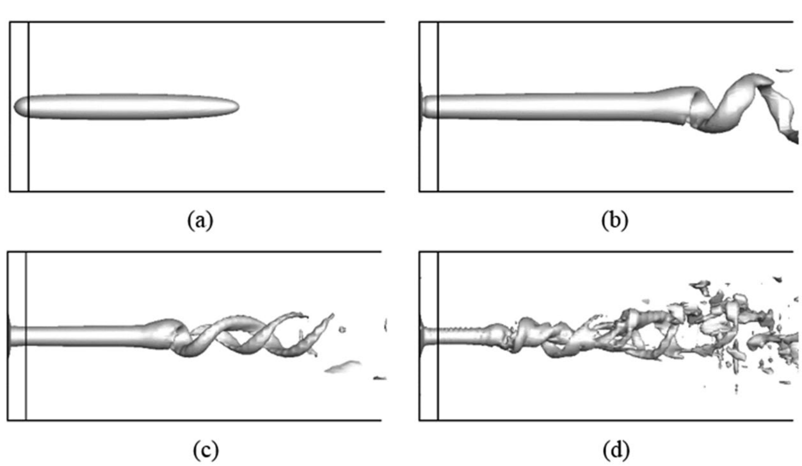

FIG. 28. Iso-surfaces of vorticity magnitude of spiral vortex breakdown at $\theta_{in} = 75°$. (a) $Re_\theta = 200$; (b) $Re_\theta = 300$; (c) $Re_\theta = 500$; (d) $Re_\theta = 1000$. The iso-surface level is different for each case.

injection angle is fixed at $\theta_{in} = 75°$. In order to demonstrate the basic features clearly, the iso-surfaces of vorticity magnitude are at different levels for the different cases. At $\mathrm{Re}_\theta = 200$, vortex breakdown does not take place. Only a straight vortex core can be observed in the flow. At $\mathrm{Re}_\theta = 300$, spiral type vortex breakdown occurs. At the stagnation point, the straight vortex core deviates from the centerline and forms a spiral pattern downstream. The flow structure rotates as a whole about the centerline with a constant frequency. When the Reynolds number increases to 500, the stagnation point of vortex breakdown shifts upstream, and the minor vortex core is created in the wake. At the same time, some random features arise in the flow. When the Reynolds number increases to 1000, the stagnation point shifts further upstream. The flow becomes more random and unstable, and small structures develop downstream. These phenomena have been extensively discussed in the literature.[9]

F. Summary of flow states and regime diagram

In this work, four types of flow patterns have been identified: columnar central recirculating zone, columnar central recirculation with longitudinal waves, bubble type vortex breakdown, and the columnar CRZ with azimuthal and longitudinal waves. The occurrence of each kind of the flow pattern is determined by the injection angle and Reynolds number.

With the development of azimuthal waves, the flow loses symmetry and rotates about the centerline. In flows in the chamber with the slip head end,[14] it was found that the propagation period of the azimuthal waves, which is also the rotation period of the flow structure, is roughly linearly dependent on the injection angle in the logarithmic scale. The time period of the accompanying longitudinal waves is approximately equal to that of the azimuthal waves for any given cases. In the flows in the chamber with viscous head end discussed in this paper, the friction on the head end has a strong influence on the flow inside. At the same time, the bouncing/restoring effects of the injected flow become important. As a result, the flow becomes much more complicated. Figure 29(a) shows the time periods of the azimuthal waves T_θ versus injection angle for different Reynolds numbers. The injection angle is given in the logarithmic scale. As in the case of the flow in the chamber with the slip head end, the plot exhibits a linear relationship between T_θ and $\log\theta_{in}$. The influence of the Reynolds number on T_θ is small.

Our simulations indicate that the time period ratio T_x/T_θ, defined as the ratio of the time period of longitudinal waves T_x to the time period of azimuthal waves T_θ, is dependent on the Reynolds number. Figure 29(b) shows the dependence of T_x/T_θ on Re_θ for different injection angles, indicating that the time period ratios fall into two categories. When Re_θ is less than a certain critical value, $T_x/T_\theta \approx 1.45$. In the higher Reynolds number range, $T_x/T_\theta \approx 1.0$. The critical Reynolds number depends on the injection angle. At a higher injection angle, the critical Reynolds number is smaller. The mechanisms of this phenomenon are not yet clear.

A complete summary of the flow types identified in this study is given in Fig. 30. Numbers are used to indicate the azimuthal wave numbers because the breakup of the free shear layer is primarily dominated by azimuthal instabilities. Previous discussions have showed that for some cases the wave number near the head end, that is, the number of preceding vortex cores, is different from that surrounding the CRZ, so we use Figs. 30(a) and 30(b) to show the flow features near the head end and around the CRZ, respectively. Figure 30(a) shows that in the low injection angle (high swirl level) range, the flow is stable to azimuthal instabilities. At a low Reynolds number, the viscous effect is so strong that no CRZ develops in the flow. With the increase in the Reynolds number, the centrifugal force becomes dominant, and this drives a columnar CRZ on the centerline. The CRZ provides the basic patterns for the other flow phenomena. When the Reynolds number further increases to a higher level, the longitudinal waves due to the solid rotation of the central flows and the axial velocity difference across the free shear layer, that is, inertial waves and longitudinally propagating Kelvin-Helmholtz waves, develop in the flow. In the high injection angle range, when the Reynolds number is not very low, the flow becomes unstable to azimuthal disturbances, and azimuthal waves develop in the free shear layer. In general, the wave number near the head end decreases with the increase in the injection angle. As the injection increases from 20° to 75°, the wave number decreases from 5 to 0. At a low Reynolds number, the free shear layer decreases to an axisymmetric vortex core, which corresponds to wave $m = 0$.

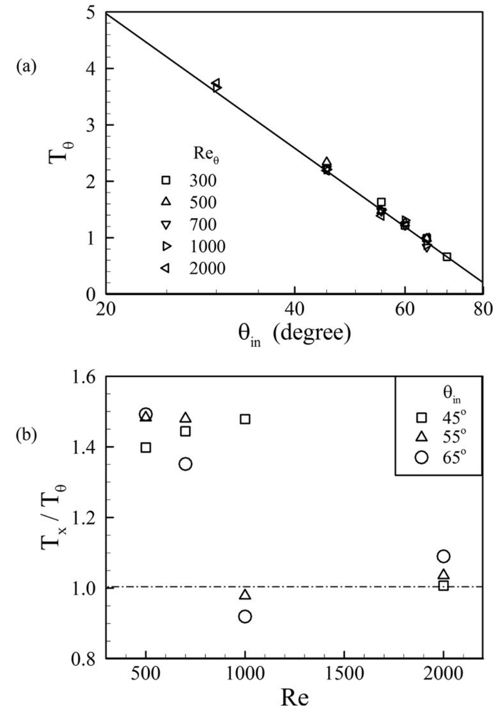

FIG. 29. Temporal features of azimuthal and longitudinal waves: (a) time period of azimuthal waves versus injection angle for different Reynolds numbers; (b) time period ratios of longitudinal waves to azimuthal waves versus Reynolds number.

Figure 30(b) shows the flow features around the CRZ. The flow pattern features remain the same in the range of low injection angles, where the azimuthal instabilities do not develop. At high injection angles, the wave number follows the trend of decreasing as the injection angle increases. The main

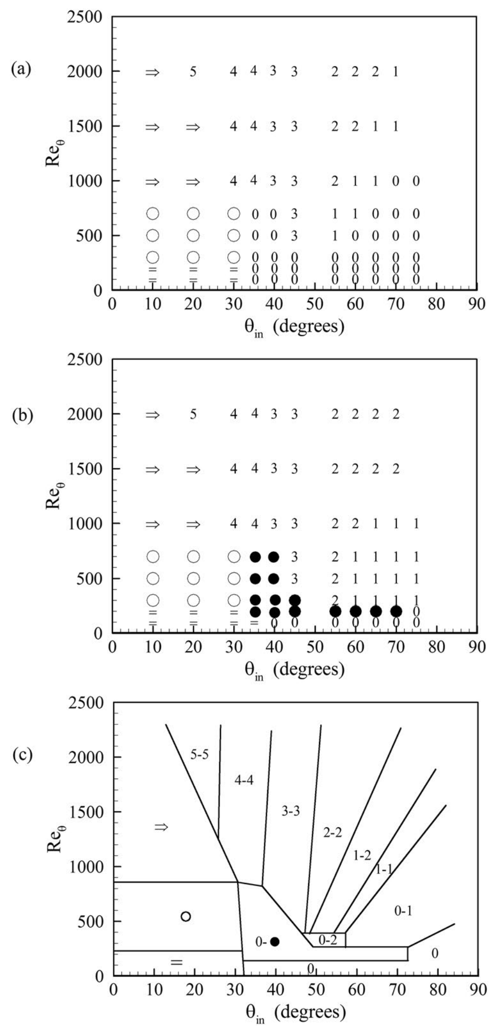

FIG. 30. Flow types identified in the cylindrical chamber. (a) Flow characteristics near the head end; (b) flow characteristics in the region around the CRZ; (c) the regime diagram of overall flow states. =: flow without the CRZ or vortex core; ○: flow with the axisymmetric CRZ; ⇒: flow with longitudinal waves embedded in the CRZ; •: flow with bubble type vortex breakdown; 0: flow with an axisymmetric vortex core (m = 0); 1: flow with an asymmetric vortex core (m = 1); #: the number of vortex cores (m = #).

differences between this figure and Fig. 30(a) are in the area of the high injection angle and low Reynolds number, where the axisymmetric vortex core ("0") near the head end expands radially to undergo bubble type vortex breakdown ("•"), and in the area where the axisymmetric vortex core ("0") in the upstream deviates from the centerline and undergoes spiral type vortex breakdown ("1"). At some other positions, this kind of change of wave number is also present.

Figure 30(c) gives the regime diagram roughly showing the overall flow states in the space of the injection angle and Reynolds number. When flow loses stability, the number before the dash represents the azimuthal wave number near the head end and that after the dash indicates the azimuthal wave number surrounding the CRZ. This figure generally shows that azimuthal stabilities only develop at higher injection angles. At a lower Reynolds number, the flow is characterized by bubble type vortex breakdown. At a higher Reynolds number, the azimuthal wave numbers in both upstream and the downstream decrease with the increase in the injection angle. The regime indicated by "0-1" represents the spiral type vortex breakdown.

V. CONCLUSIONS

By studying the flow characteristics of swirling flow in a cylindrical chamber over a broad range of Reynolds numbers and injection angles, we systematically investigated the mechanisms of transition between different flow states from the perspective of instability waves, and we have developed a unified theory connecting the distinct flow phenomena. Through comprehensive analysis, it was found that the formation of each flow state is the result of interaction and competition among a few basic mechanisms: (1) the centrifugal effect, which drives an axisymmetric CRZ in swirling flow, (2) flow instabilities developing at the free shear layer and the central solid-body rotating flow, (3) the bouncing and restoring effects of the injected flow, which facilitate the convergence of flow on the centerline and the formation of bubble type vortex breakdown, and (4) the damping effect of the end-induced flow, which suppresses the development of the instability waves.

At a low injection angle (high swirl level), the centrifugal force drives a columnar CRZ on the centerline. The end-induced flow separates the CRZ from the head end and the outer main flow. A free shear layer develops between the outer main flow and the CRZ. Inertial waves due to solid-body rotation of the central flow, and longitudinally propagating Kelvin-Helmholtz waves, develop at the free shear layer when the Reynolds number increases up to a certain value. In the medium and high injection angle (medium and low swirl level) range, the radial impingement of injected flow becomes stronger, and this pushes the circular free shear layer to the centerline. At a low Reynolds number, the free shear layer decreases to an axisymmetric vortex core on the centerline. Due to the flow viscosity and the damping of end-induced flow, no flow reversal is created in the flow. When the Reynolds number increases up to a certain level, the bouncing and restoring effects of injected flow take effect, and this creates a recirculation bubble in the upstream region and triggers bubble type vortex breakdown. The symmetric preceding vortex core expands radially and becomes the circular free shear layer on the front surface of the vortex breakdown bubble. As the Reynolds number further increases to a higher level, a CRZ arises downstream. Flow becomes unstable to azimuthal disturbances, and the free shear layer rolls up to form a number of spiral vortex cores. Kelvin-Helmholtz type azimuthal waves develop in the flow due to the sharp change of azimuthal velocity across the free shear layer. Due to the damping effect of the end-induced flow, the azimuthal wave number near the head end is smaller than that in the downstream region for some cases. By and large, the azimuthal wave number decreases with an increase in the injection angle, as a result of the reduction in the perimeter of the cylindrical free shear layer. On the other hand, the increase in the Reynolds number tends to increase the wave number. When the injection angle becomes so high that the azimuthal wave number decreases to $m = 0$ near the head end and $m = 1$ downstream, the commonly observed spiral vortex breakdown takes place.

It can be concluded that the CRZ, together with the free shear layer on its surface, composes the basic structure of swirling flow. The instability waves developing in the flow interact with the injected flow and the end-induced flow and create a number of complex wave phenomena. The dominant wave mode is primarily determined by the injection angle and Reynolds number. Spiral type vortex breakdown is a limiting case at high injection angle, with wave number equal to 0 near the head end and equal to 1 in the downstream. At a lower Reynolds number, the bouncing and restoring effect of the injected flow generates bubble type vortex breakdown.

ACKNOWLEDGMENTS

This work was sponsored partly by the Air Force Office of Scientific Research under Grant No. FA 9550-10-1-0179 and partly by the William R. T. Oakes Endowment of the Georgia Institute of Technology. The authors gratefully acknowledge the support and advice from Mitat A. Birkan.

[1] N. Syred and J. M. Beer, "Combustion in swirling flows: A review," Combust. Flame **23**, 143–201 (1974).
[2] A. K. Gupta, D. G. Lilley, and N. Syred, *Swirl Flows* (Abacus Press, 1984).
[3] Y. Huang and V. Yang, "Dynamics and stability of lean-premixed swirl-stabilized combustion," Prog. Energy Combust. Sci. **35**, 293–364 (2009).
[4] D. H. Peckham and S. A. Atkinson, "Preliminary results of low speed wind tunnel test on a Gothic wing of aspect ratio 1.0," A. R. C. Technical Report C.P. No. 508, TN No. Aero. 2504, 1957.
[5] J. H. Faler and S. Leibovich, "Disrupted states of vortex flow and vortex breakdown," Phys. Fluids **29**, 1385–1400 (1977).
[6] D. J. C. Dennis, C. Seraudie, and R. J. Poole, "Controlling vortex breakdown in swirling pipe flows: Experiments and simulations," Phys. Fluids **26**, 053602 (2014).
[7] S. W. Wang, S. Y. Hsieh, and V. Yang, "Unsteady flow evolution in swirl injector with radial entry. I. Stationary conditions," Phys. Fluids **17**, 045106 (2005).
[8] S. W. Wang and V. Yang, "Unsteady flow evolution in swirl injectors with radial entry. II. External excitations," Phys. Fluids **17**, 045107 (2005).
[9] O. Lucca-Negro and T. O'Doherty, "Vortex breakdown: A review," Prog. Energy Combust. Sci. **27**, 431–481 (2001).
[10] X. Wang, Y. Wang, and V. Yang, "Geometric effects on liquid oxygen/kerosene bi-swirl injector flow dynamics at supercritical conditions," AIAA J. **55**, 3467–3475 (2017).
[11] X. Wang, H. Huo, Y. Wang, and V. Yang, "Comprehensive study of cryogenic fluid dynamics of swirl injectors at supercritical conditions," AIAA J. **55**, 3109–3119 (2017).
[12] J. K. Harvey, "Some observations of the vortex breakdown phenomenon," J. Fluid Mech. **14**, 585–592 (1962).
[13] B. T. Vu and F. C. Gouldin, "Flow measurements in a model swirl combustor," AIAA Paper No. 80-0076, 1980.
[14] Y. Wang and V. Yang, "Central recirculation zones and instability waves in internal swirling flows with tangential entry," Phys. Fluids (to be published).
[15] A. Kovacs and M. Kawahara, "A finite element scheme based on the velocity correction method for the solution of the time-dependent incompressible Navier-Stokes equations," Int. J. Numer. Methods Fluids **13**, 403–423 (1991).
[16] Y. Wang, X. Lu, and L. Zhuang, "Numerical analysis of the rotating viscous flow approaching a solid sphere," Int. J. Numer. Methods Fluids **44**, 905–925 (2004).
[17] Y. Wang, X. Lu, L. Zhuang, Z. Tang, and W. Hu, "Numerical simulation of drop Marangoni migration under microgravity," Acta Astronaut. **54**, 325–335 (2004).
[18] R. Hide and C. W. Titman, "Detached shear layers in a rotating fluid," J. Fluid Mech. **29**, 39–60 (1967).
[19] G. K. Batchelor, *An Introduction to Fluid Dynamics* (Cambridge University Press, 2000).
[20] M. P. Escudier, "Observations of the flow produced in a cylindrical container by a rotating endwall," Exp. Fluids **2**, 189–196 (1984).
[21] J. M. Lopez, "Axisymmetric vortex breakdown Part 1. Confined swirling flow," J. Fluid Mech. **221**, 533–552 (1990).
[22] M. P. Escudier, J. Bornstein, and N. Zehnder, "Observations and LDA measurements of confined turbulent vortex flow," J. Fluid Mech. **98**, 49–63 (1980).